# Stardust Interstellar Preliminary Examination XI: Identification and elemental analysis of impact craters on Al foils from the Stardust Interstellar Dust Collector

Rhonda M. STROUD[1], Carlton ALLEN[2], Asna ANSARI[3], David ANDERSON[4], Saša BAJT[5], Nabil BASSIM[1], Ron S. BASTIEN[6], Hans A. BECHTEL[7], Janet BORG[8], Frank E. BRENKER[9], John BRIDGES[10], Donald E. BROWNLEE[11], Mark BURCHELL[12], Manfred BURGHAMMER[13], Anna L. BUTTERWORTH[4], Hitesh CHANGELA[1,14], Peter CLOETENS[13], Andrew M. DAVIS[15], Ryan DOLL[16], Christine FLOSS[16], George FLYNN[17], David R. FRANK[6], Zack GAINSFORTH[4], Eberhard GRÜN[18], Philipp R. HECK[3], Jon K. HILLIER[19], Peter HOPPE[20], Joachim HUTH[20], Brit HVIDE[3], Anton KEARSLEY[21], Ashley J. KING[15], Paul KOTULA[22], Barry LAI[23], Jan LEITNER[20], Laurence LEMELLE[24], Hugues LEROUX[25], Ariel LEONARD[16], Robert LETTIERI[4], William MARCHANT[3], Larry R. NITTLER[26], Ryan OGLIORE[27], Wei Jia ONG[16], Frank POSTBERG[19], Mark C. PRICE[12], Scott A. SANDFORD[28], Juan-Angel Sans TRESSERAS[13], Sylvia SCHMITZ[9], Tom SCHOONJANS[29], Kate SCHREIBER[16], Geert SILVERSMIT[29], Alexandre S. SIMIONOVICI[30], Vicente A. SOLÉ[13], Ralf SRAMA[18,31], Thomas STEPHAN[15], Veerle J. STERKEN[32], Julien STODOLNA[4], Steven SUTTON[23], Mario TRIELOFF[19], Peter TSOU[33], Akira TSUCHIYAMA[34], Tolek TYLISZCZAK[7], Bart VEKEMANS[29], Laszlo VINCZE[28], Andrew J. WESTPHAL[4], Joshua VON KORFF[4], Daniel ZEVIN[4], and Michael E. ZOLENSKY[2]

[1]Materials Science and Technology Division, Naval Research Laboratory,
Washington, District of Columbia, USA
[2]ARES, NASA Johnson Space Center, Houston, Texas, USA
[3]Robert A. Pritzker Center for Meteoritics and Polar Studies,
The Field Museum of Natural History, Chicago, Illinois, USA
[4]Space Sciences Laboratory, U.C. Berkeley, Berkeley, California, USA
[5]DESY, Hamburg, Germany
[6]JETS, NASA Johnson Space Center, Houston, Texas, USA
[7]Advanced Light Source, Lawrence Berkeley Laboratory, Berkeley, California, USA
[8]IAS Orsay, Orsay, France
[9]Institut für Geowissenschaften, Goethe Universität, Frankfurt am Main, Germany
[10]Space Research Centre, University of Leicester, Leicester, UK
[11]Department of Astronomy, University of Washington, Seattle, Washington, USA
[12]University of Kent, Canterbury, Kent, UK
[13]European Synchrotron Radiation Facility, Grenoble, France
[14]George Washington University, Washington, District of Columbia, USA
[15]University of Chicago, Chicago, Illinois, USA
[16]Washington University, St. Louis, Missouri, USA
[17]SUNY Plattsburgh, Plattsburgh, New York, USA
[18]Max-Planck-Institut für Kernphysik, Heidelberg, Germany
[19]Institut für Geowissenschaften, University of Heidelberg, Heidelberg, Germany
[20]Max-Planck-Institut für Chemie, Mainz, Germany
[21]Natural History Museum, London, UK
[22]Sandia National Laboratory, Albuquerque, New Mexico, USA
[23]Advanced Photon Source, Argonne National Laboratory, Chicago, Illinois, USA
[24]ENS, Lyon, France
[25]Université des Sciences et Technologies, de Lille, France
[26]Carnegie Institution of Washington, Washington, District of Columbia, USA
[27]University of Hawaii at Manoa, Honolulu, Hawaii, USA
[28]NASA Ames Research Center, Moffett Field, California, USA

[29]University of Ghent, Ghent, Belgium
[30]Institut des Sciences de la Terre, Observatoire des Sciences de
l'Univers de Grenoble, Grenoble, France
[31]IGEP, TU Braunschweig, Braunschweig, Germany
[32]IRS, University Stuttgart, Stuttgart, Germany
[33]Jet Propulsion Laboratory, Pasadena, California, USA
[34]Osaka University, Osaka, Japan
[*]Corresponding author. E-mail: stroud@nrl.navy.mil

**Abstract**–The Stardust Interstellar Preliminary Examination team analyzed thirteen Al foils from the NASA Stardust interstellar collector tray in order to locate candidate interstellar dust (ISD) grain impacts. Scanning electron microscope (SEM) images reveal that the foils possess abundant impact crater and crater-like features. Elemental analyses of the crater features, with Auger electron spectroscopy, SEM-based energy dispersive X-ray (EDX) spectroscopy, and scanning transmission electron microscope-based EDX spectroscopy, demonstrate that the majority are either the result of impacting debris fragments from the spacecraft solar panels, or intrinsic defects in the foil. The elemental analyses also reveal that four craters contain residues of a definite extraterrestrial origin, either as interplanetary dust particles or ISD particles. These four craters are designated level 2 interstellar candidates, based on the crater shapes indicative of hypervelocity impacts and the residue compositions inconsistent with spacecraft debris.

## INTRODUCTION

The NASA Stardust spacecraft carried two dust collection trays: one for capture of dust from comet 81P/Wild 2, and one for capture of contemporary interstellar dust (ISD) (Tsou et al. 2003). Whereas the successful capture of Wild 2 grains was readily apparent from the first direct visual observations of the cometary collector tray (Brownlee et al. 2006), achieving a reasonable level of confidence that detectable interstellar grains were captured in the ISD collector tray has required a multiyear, multifaceted preliminary examination research campaign. The primary reason that locating the returned ISD samples is so challenging compared to locating the cometary grains is the combination of low total particle fluence and small particle size. Prior to return of the Stardust samples, the total number of ISD particles likely to be captured on the entire tray was estimated to be 120, with 2/3 smaller than 2 μm in diameter, based on data from the Ulysses and Galileo missions (Landgraf et al. 1999). Landgraf et al. (1999) also predicted capture of interplanetary particles, but at significantly lower fluence, yielding a total of 20 total larger than 0.6 μm diameter. Any captured particles would form a random distribution across the total 0.1 m$^2$ exposed area of the ISD collector tray, which comprises approximately 85% aerogel and approximately 15% Al foil surfaces. Furthermore, secondary ejecta from the spacecraft, i.e., debris fragments

produced by a micrometeoroid impact to the solar cell array or other parts of the spacecraft, were also collected on the tray, providing a large background of noninterstellar impact features (Burchell et al. 2012). Thus, locating any captured ISD particles involves acquisition and careful inspection of tens to hundreds of thousands of high-resolution optical and electron microscope images. Nonetheless, the Stardust samples are the first opportunity for direct laboratory measurements of contemporary ISD, and as such, potentially provide unprecedented constraints for models of the composition and structure of the dust in the local interstellar medium. For this reason, the Stardust Interstellar Preliminary Examination (ISPE) team was assembled and tasked with locating the few, but precious, captured dust grains on the interstellar tray. A detailed description of the scope and limitations of the ISPE is given by Westphal et al. (2014). Results from the preliminary analysis of the interstellar collector foil samples, which support the identification of four candidate interstellar impact craters, are presented herein. Additional analyses supporting the identification of three candidate interstellar particles in the aerogel samples are presented elsewhere in the eleven companion papers, ISPE0-ISPEX.

The Al foils on the collector trays serve a dual purpose. They were designed primarily as shims, to minimize the risk that the brittle aerogel tiles might fracture on removal from the tray, and only secondarily

as sample collection media (Tsou et al. 2003). The Al alloy used for the foils was $Al_{1100}$, which is >99 wt% Al, with <0.95 wt% Si+Fe, <0.2 wt% Cu, <0.05 wt% Mn, and <0.1 wt% Zn. However, sub-μm to μm-sized Fe, Ti, and Si-rich inclusions are present in the foil (Kearsley et al. 2007; Leroux et al. 2008), in addition to numerous surface scratches. Despite these complications, the foils are much easier to analyze for sub-μm grain impacts than are the aerogel tiles. Unlike the aerogel, the Al foils are conducive to automated imaging with scanning electron microscopy (SEM) at spatial resolutions down to a few nanometers; the residues of the captured particles are confined to the foil surface for easier chemical analysis and contamination with melted silica aerogel is minimal to nonexistent. Studies of impact craters from the cometary tray have shown that primary mineralogy and isotopic compositions can be retained in the foil-captured samples, at least for impacts with an encounter speed of 6.1 km s$^{-1}$ (Hörz et al. 2006; McKeegan et al. 2006; Leroux et al. 2008; Stadermann et al. 2008; Wozniakiewicz et al. 2012).

Besides the small size and low number of particles, Landgraf et al. (1999) predicted another major challenge in the analysis of the captured ISD. Based on the average speed of the ISD stream calculated from Ulysses and Galileo data, and the velocity of the Stardust spacecraft, the expected average capture speed of the ISD on the Stardust collector tray was >20 km s$^{-1}$. At this speed, much more severe alteration of captured particles was expected for both those in aerogel and those on the foils, in comparison with that experienced by the cometary dust samples. In anticipation of these high capture speeds, laboratory and computer simulation studies (Price et al. 2012) were performed to determine the morphological features of such impact craters. It was determined that the craters in Al foil from approximately 20 km s$^{-1}$ grain impacts are larger in both diameter and depth, whereas the volume of retained residue is smaller than for 6.1 km s$^{-1}$ impacts. Methods for noninvasive microanalysis of the residue compositions from these high-velocity impacts were also tested, including energy dispersive X-ray spectroscopy (EDX), Auger electron spectroscopy (Stadermann and Floss 2008), and synchrotron-based photoelectron emission microscopy (Ogliore et al. 2010). Auger spectroscopy provided the best combination of imaging resolution for locating the feature for analysis with greatest surface sensitivity for chemical measurements. It was demonstrated that for some oblique impacts, Auger spectroscopy could detect the asymmetric distribution of residue outside the crater rim that could be used for constraining the trajectory of the captured dust grain (Stadermann et al. 2010), and

possibly inferring the origin, e.g., secondary ejecta from the spacecraft's solar panel.

Most of the available data from the laboratory simulation impact studies pertain to projectile particles >1 μm in diameter (Postberg et al. 2011; Price et al. 2012). This is because monodisperse standard samples are more readily obtained for sizes >1 μm, and these are easier to accelerate by both light-gas gun (Price et al. 2012) and Van de Graaf accelerators (Postberg et al. 2011). Recent extension of the light-gas gun studies to the sub-μm projectile regime shows that the linear relationship between crater diameter ($D_c$) and projectile diameter ($D_p$) has a discontinuity at $D_p \approx 2.4$ μm (Price et al. 2010). For spherical particles with a density of 2.4 g cm$^{-3}$ and diameter $D_p > 2.4$ μm at impact speeds of 6 km s$^{-1}$, $D_c \sim 4.62 \times D_p$. For $D_p < 2.4$ μm, $D_c \sim 1.60 \times D_p$. This means that caution must be exercised when extrapolating directly from the simulations involving large grains in the interpretation of sub-μm grain impact crater features. However, the extensive data from the analysis of sub-μm craters on the cometary collector tray foils are an important aid for interpretation of the impacts on the interstellar tray. Data from SEM (Borg et al. 2007; Price et al. 2010) and NanoSIMS analysis (Stadermann et al. 2008; Leitner et al. 2010a; Heck et al. 2012) of several hundred impact craters from the cometary trail are available. Transmission electron microcopy (TEM) data from approximately 10 μm to sub-μm cometary dust impact craters (Leroux et al. 2010; Stroud et al. 2010a) are also available. These data show that analyzable residue is retained even for craters as small as 0.25 μm diameter, if the impact speed is close to that of the cometary encounter, i.e., 6.1 km s$^{-1}$. In addition, the variation of the sub-μm cometary crater depth:diameter ratio from 0.5 to 1, demonstrates that this ratio depends on the particle microstructure and composition as much as impact speed. It should be noted that laboratory studies of particles ≥50 μm show very different relationships between crater depth and velocity, with deep craters occurring at very low velocity, and shallow craters occurring at high velocity (see Hörz 2012; fig. 3).

Although extensive work has gone into predicting the amount and type of dust that was collected, and toward providing context for interpretation of impact features, much of the work relies on assumptions regarding the properties of sub-μm cosmic dust itself. The optical properties of individual sub-μm interstellar and interplanetary dust particles, i.e., infrared absorption and response to solar light pressure, their compositions, morphology (simple or porous aggregates), and velocities are all poorly constrained. The analyses of returned dust presented in this and the companion papers in this volume are an important test of the validity of these assumptions.
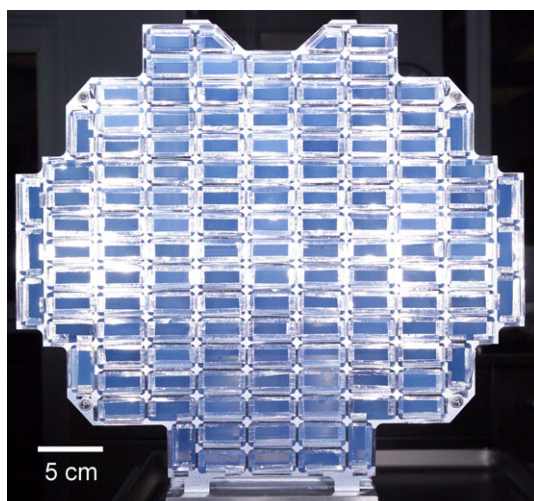
Fig. 1. Optical image of the Stardust Interstellar tray. The Al foils, which were folded over the ribs of the tray to serve as shims for securing and removing the aerogel tiles, account for approximately 15% of the total exposed collection surface.
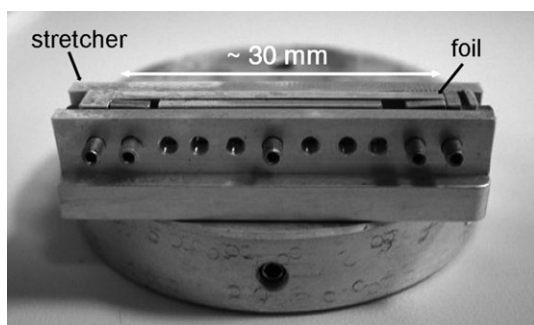


Fig. 2. Side view optical image of an extracted long foil, mounted in an archival stretcher that is resting on a scanning electron microscope pin-mount holder.

## METHODS

### Samples

Curatorial staff at Johnson Space Center extracted individual Al foils from the Stardust interstellar tray (Fig. 1) with the double-blade rolling cutter, first developed for harvesting of foils from the Stardust cometary tray (Kearsley et al. 2008). In order to minimize the risk of damage to any tracks in the aerogel tiles, individual foils were cut after high-resolution optical images of the adjacent aerogel tiles were obtained. The foil strips were then mounted onto custom-designed Al mounts at the Space Sciences Laboratory at UC Berkeley. These custom mounts clamp the foil at each end, permitting the foil to be stretched for greater flatness and, thus, easier imaging (Fig. 2). The mounts have a 0.125 inch pin that is compatible with conventional SEM sample stages.
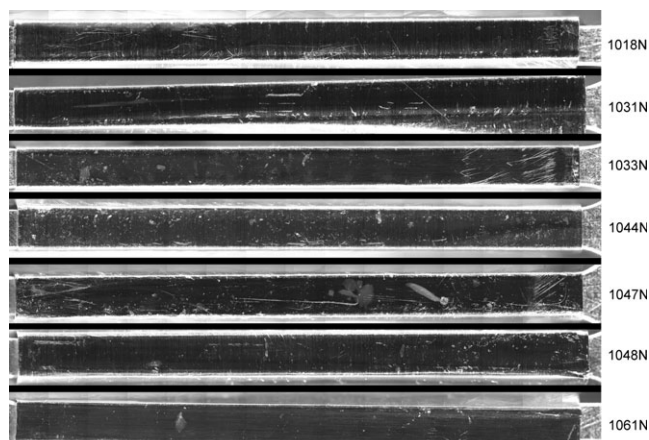


Fig. 3. Composite of level II documentation optical images (see http://curator.jsc.nasa.gov/stardust/sample_catalog/Interstellar/Level2/Interstellar_Foil_Map.html) of the seven long foils mapped for this study.
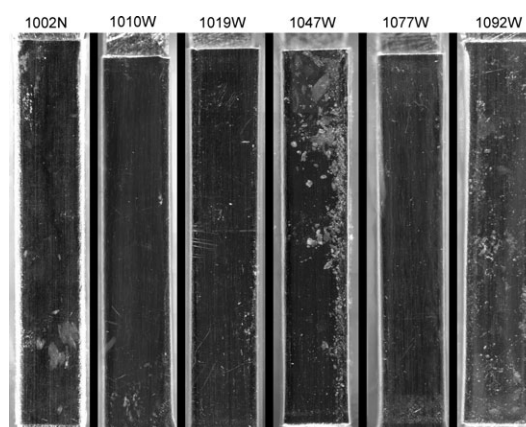


Fig. 4. Composite of level II documentation optical images of the six short foils mapped for this study.

Fifteen foils were distributed to participating institutions for automated SEM imaging: Carnegie Institution of Washington (CIW), 1092W,1 and 1018N,1; the Field Museum (FM), 1033N,1 and 1002N,1; the Max Planck Institute for Chemistry (MPI), 1044N,1 and 1019W,1; the Naval Research Laboratory (NRL), 1077W,1 and 1010W,1; the University of Leicester (UL), 1047W,1 and 1048N,1; and Washington University in St. Louis (WUSTL), 1061N,1, 1031N,1, 1032W,1, 1047N,1, and 1063W,1. The sample naming convention for the foils is tile number followed by N for north or W for west, respectively. Most of the north foils are 33.6 mm in length (Fig. 3), and the west foils are 12.7 mm (Fig. 4). At outer edges of the tray, the cell orientation is rotated 90° so that the north foils are 12.7 mm and the west foils are 33.6 mm in length (Fig. 1). The width of the

Table 1. Summary of foils analyzed.

| Foil | Area[a] (cm$^2$) | Total # of crater features/secondaries[b] | Feature density (cm$^{-2}$) | 1σ Confidence range of secondary crater density[c] (cm$^{-2}$) |
|---|---|---|---|---|
| 1061N,1 | ~0.65* | 7/1–4 | 11 | 0.26–11 |
| 1031N,1 | ~0.51* | 4/2–4 | 5 | 1.34–14 |
| 1044N,1 | ~0.50 | 4/3 | 8 | 2.6–12 |
| 1092W,1 | ~0.28 | 2/2 | 7 | 2.5–4.6 |
| 1077W,1 | ~0.12 | 2/1 | 17 | 5.8–38 |
| 1047W,1 | ~0.17 | 0/0 | 0 | 0–11 |
| 1047N,1 | ~0.66* | 1/0 | 2 | 0–2.8 |
| 1010W,1 | ~0.14 | 1/0 | 7 | 0–24 |
| 1018N,1 | ~0.24* | 1/0 | 4 | 0–7.5 |
| 1019W,1 | ~0.2 | 1/1 | 5 | 0.9–17 |
| 1033N,1 | ~0.67 | 2/1 | 3 | 0.3–4.9 |
| 1048N,1 | ~0.50 | 0/0 | 0 | 0–3.6 |
| 1002N,1 | ~0.20 | 0/0 | 0 | 0–9.2 |

[a]Foil area indicated with "*" is analyzed area, not total foil area.
[b]The total number of crater features identified includes primary and secondary impacts, and crater-like defects in the foils.
[c]The 1σ confidence range of secondary crater areal density is calculated as the 1σ confidence interval (Gehrels 1986) of the number of secondary impacts on each foil, normalized to the analyzed area. For foils in which the number of secondaries is listed as a range, the confidence range spans the lower limit for the lowest count to the highest limit for the highest count.

exposed area of the foils, as mounted on the tray on top of the Al ribs, is approximately 0.2–0.3 mm wider than the 2.33 mm ribs. Both the foil cutting and the mounting on the stretchers results in a reduction of the searchable foil area. Typical foil strips are 1.7–2 mm wide after cutting from the tray (Kearsley et al. 2008). The realistic total searchable foil area is approximately 100 cm$^2$, 2/3 of the nominal 150 cm$^2$ exposed area (Table 1).

**Carbon Contamination Monitoring**

To guard against the possibility of excessive carbon build-up on the foils during SEM imaging, which could be detrimental to subsequent Auger spectroscopy (Kearsley et al. 2010) or other surface sensitive analyses, a protocol to test the C contamination rate of individual instruments was developed. The protocol is based on energy dispersive X-ray spectroscopy measurements of the ratio of the C $K_\alpha$ peak intensity to the Al $K_\alpha$ intensity, which is a function of C coating thickness, for a given set of operating conditions. The protocol was validated with a suite of carbon films deposited onto an Al 99.99% foil in an Edwards AUTO306 coating system at the Natural History Museum (NHM) in London (Fig. 5a). The first foil, with three intact carbon coat layers, was sectioned by focused ion beam (FIB) milling at Imperial College London, and the coating thicknesses measured on a Hitachi TEM at NHM. SEM-EDX spectra were then collected from broad areas on the surface of the coated foils under strictly controlled conditions of electron beam current and energy. The raw spectral histogram data (e.g., Fig. 5b) were processed using the Oxford Instruments INCA software to separate peaks from background, and the ratio of C to Al X-ray counts was plotted against the known coat thickness, revealing a linear relationship for these relatively thick C layers (Fig. 5c). Two further sets of C coat standards were produced in a Cressington 208 C coater at NHM, with the precise thickness of each layer monitored by a Cressington mtm10 thickness monitor. This extended the calibration to overlap with data for very thin layers (1.5 nm and greater), which again showed a linear trend of C/Al counts when analyzed at high accelerating voltage (20 kV, Fig. 5d), but a slightly more complex trend at low voltage (5 kV).

The trend of C/Al values for calibrated C thickness was then applied to data acquired from a "dirty" SEM instrument with rotary and oil-diffusion vacuum pumps, already known to deposit substantial contamination. Measurements were repeated under a wide range of known beam current (100 pA to 10 nA) and accelerating voltage (5–20 kV) conditions, to determine their influence on the rate of contamination deposition. In each experiment, the electron beam was continuously scanned across a small area (approximately 4 μm × 3 μm) of high purity Al foil, whilst repeated EDX spectra were collected, for example 40 consecutive spectra, each of 50 s "live time." The spectra were then processed to obtain C/Al count values, which were converted to equivalent carbon coating thickness and plotted against the total beam irradiation time per square micrometer of the foil. There was no statistically
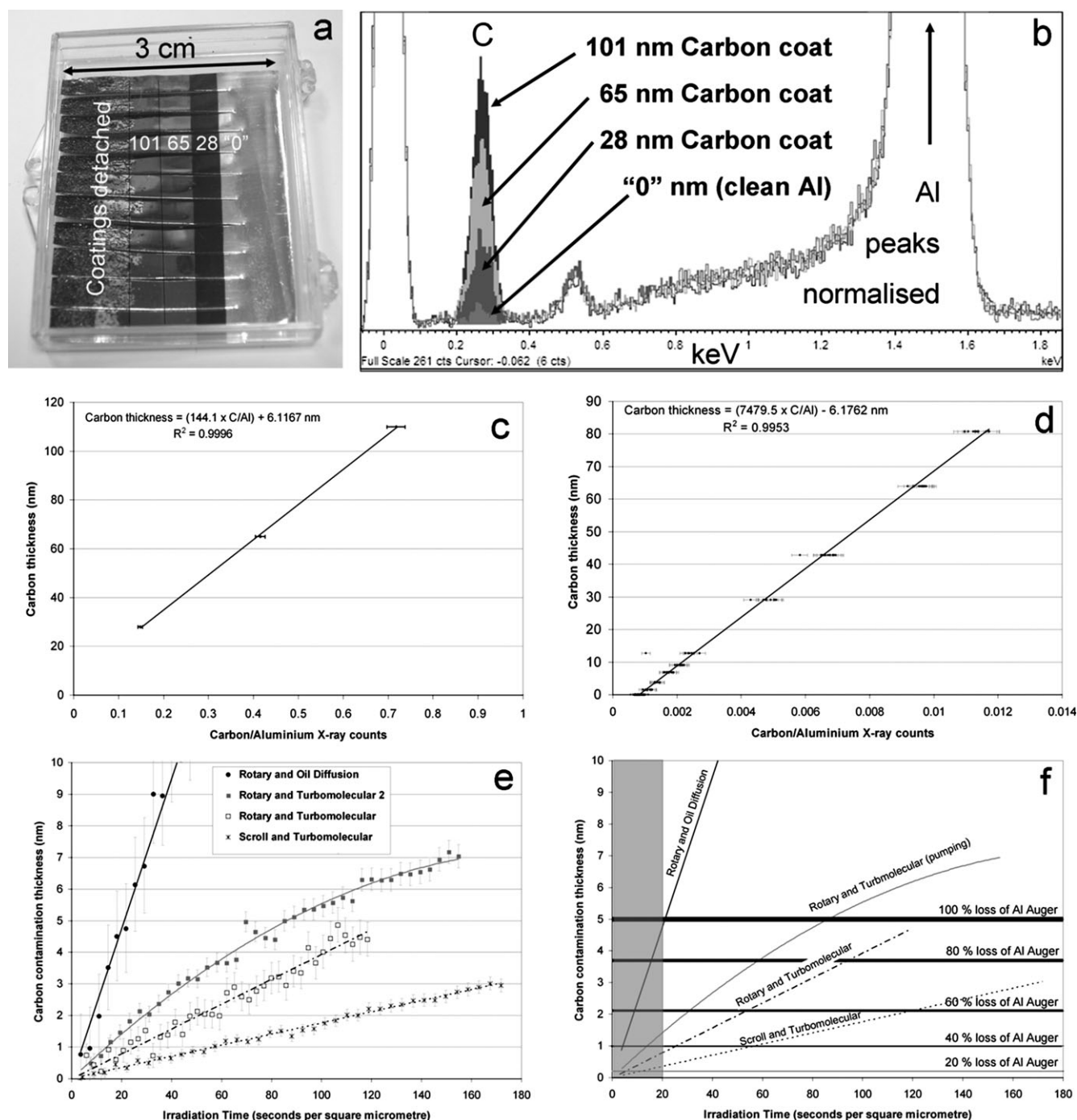
Fig. 5. Carbon contamination monitoring in the SEM. a) strips of high purity aluminum (Al) foil with known thickness layers of carbon (C) coating, used as contamination calibration standards for measurement of C and Al X-ray counts by EDX detectors; b) example EDX spectra from the calibration standards; c) plot of C/Al X-ray counts versus thickness of 3 standard carbon coatings, 5 kV 1 nA, as used for calibration in this study, error bars are 3 standard deviation maxima and minima, from statistics of peak above background count detection limits; d) plot of C/Al X-ray counts versus thickness for a wide range of standard carbon coatings, 20 kV 2 nA; e) measured contamination accumulation as a function of foil irradiation time for four different SEM instruments; f) contamination as in e), with thresholds for loss of Al Auger signal shown as horizontal lines. The gray band indicates the irradiation time in an oil pumped SEM that results in 100% loss of Auger signal of the Al foil due to carbon contamination build-up.

significant difference between the rate of contamination seen in measurements at different accelerating voltage or beam current on this instrument, suggesting that these parameters did not exert a significant control on the rate of deposition.

Test samples of smooth, high purity Al foil with C coats of known thickness were distributed by NHM to each participating institution, and the same assessment protocol was then used to document contamination rates in instruments that were used for crater searching. To give a safety margin it was decided that imagery should be confined to dwell times of less than $0.1$ s $\mu m^{-2}$, with an average contamination thickness of less than a monolayer of carbon. All of the instruments used in ISPE easily met the cleanliness criterion. Thus, the greatest potential source of carbon contamination during imaging was from mobilization and redeposition of pre-existing hydrocarbons from the foils themselves. To preserve a record of the carbon contamination rate for each foil imaging session, witness areas were imaged on separate, precleaned Al stubs, designated sections of the foil stretcher, or crater-free regions of the foil.

### Automated Imaging and Crater Identification

Foil 1077W,1 (Stroud et al. 2010b, 2011) was mapped at NRL at a nominal resolution of $40$ nm $px^{-1}$, with a JEOL 7101 VP field-emission SEM equipped with EDAX Genesis stage automation software. The operating voltage was 15 kV, at working distance of 10 mm, beam current <1 nA, and total image integration time of 15 s. Each 8-bit $2048 \times 1600$ px image spanned $82$ $\mu m \times 64$ $\mu m$ of the foil. Foil 1010W,1 was mapped at NRL with an FEI Nova 600 FIB-SEM operated under control of a custom automation script. The operating conditions were 5 kV and a 5 mm working distance. Candidate craters were identified by manual image searching, as well as with automated software (Ogliore et al. 2012). High-probability candidates were re-imaged at a nominal $15$ nm $px^{-1}$ resolution.

Foils 1092W,1 and 1018N,1 were mapped at CIW, at a nominal resolution of $46$ nm $px^{-1}$, with a JEOL 6500F FE-SEM and EDAX Genesis stage automation software. The SEM operating conditions were: 10 kV, 10 mm working distance, and 2 nA probe current. Individual 12-bit images of size $94$ $\mu m \times 73$ $\mu m$ were acquired with an integration time of 15 s per image. Candidate craters were identified using automated image search routines (Ogliore et al. 2012), and re-imaged at 15 kV and a $15$ nm $px^{-1}$ nominal resolution.

Foils 1044N,1 and 1019W,1 were imaged at MPI with a LEO1530 FE-SEM and Point Electronics stage automation software at a nominal resolution of approximately $60$ nm $px^{-1}$, at an acceleration voltage of 5 kV, beam current of <1 nA, and working distance of 5–9 mm (Leitner et al. 2010b). Individual images were $60$ $\mu m \times 60$ $\mu m$ ($1000 \times 1000$ px at 8 bit grayscale) in size, with an integration time of 14 s (i.e., $0.0039$ s $\mu m^{-2}$). Candidate craters were identified by manual searching and re-imaged at $20$ nm $px^{-1}$ nominal resolution.

Foils 1061N,1, 1031N,1, 1032W,1, 1047N,1, 1063W,1 were mapped at WUSTL, with a JEOL 840a SEM equipped with Noran System Seven software for automated image acquisition (Floss et al. 2010, 2011). The scanning protocol consisted of acquisition of individual images of $106$ $\mu m \times 80$ $\mu m$ ($2048 \times 1536$ px at 16 bit grayscale) at 15 kV, 5 nA for 10 s per frame, providing a resolution of approximately $52$ nm $px^{-1}$ with a dwell time of $0.002$ s $\mu m^{-2}$. Verification of crater candidates was carried out with our PHI 700 Auger Nanoprobe equipped with a field emission electron source. Mapping parameters were similar to those used for the automated searches, but images were scanned at a higher resolution of approximately $15$ nm $px^{-1}$.

Foils 1047W,1 and 1048N,1 were mapped at UL, with a Hitachi S-3600N SEM, operated at 15 kV, 10 mm working distance and measured beam current approximately 0.3–0.5 nA. The nominal resolution was $60$ nm $px^{-1}$. Each $2048 \times 1408$ px image spanned $120$ $\mu m \times 83$ $\mu m$. Because no craters were identified from the initial images series of either foil, 1048N,1 was re-imaged at NRL, with the FEI Nova 600 FIB-SEM. These images were searched manually and with the automated search software.

Foils 1033N,1 and 1002N,1 were imaged at the FM in Chicago, with a Zeiss Evo 60 SEM at a nominal resolution of $52$ nm $px^{-1}$. The operating conditions were 15 kV, at a working distance of 9–10 mm, and 170–240 pA beam. The images were $2048 \times 1536$ px at 8 bit depth. Crater candidates were identified by manual searching of the images, and re-imaged at a nominal resolution of $18$ nm $px^{-1}$. In addition, high-resolution re-imaging was required to distinguish crater candidates from foil impurities or artifacts. Candidates on foil 1033N,1, were re-imaged with the FEI Nova 600 FIB-SEM at NRL and candidates on foil 1002N,1 with a Hitachi S-4700 II FESEM at Argonne National Laboratory.

### Elemental Analysis

Because the composition and thickness of any retained impactor residue was highly uncertain at the start of the preliminary examination, no single elemental analysis technique could be used for

nondestructive residue detection with 100% confidence. Thus, the elemental analyses of the crater candidates (see Table 3) were performed in two separate rounds following three distinct measurement protocols. In the first round of analyses, three craters (7, 18, 21) were analyzed with AES, one (14) with a conventional, off-axis, Si(Li) EDX in a field emission SEM, and two (4, 24) with a custom on-axis, annular silicon drift detector (SDD) EDX spectrometer in a field emission SEM. Four (4, 7, 21, 24) of these craters that contained residue not obviously terrestrial in composition were subsequently prepared for scanning transmission electron microscopy (STEM), with FIB lift-out methods. Based on the results from the first-round analyses, it was determined that the Auger spectroscopy, conventional and on-axis SDD-EDX measurements could each nondestructively detect residue, but that in some cases STEM-EDX was required to rule out spacecraft debris. For the second round, the following measurements of additional craters were authorized: ten by Auger, four by conventional Si(Li) SEM-EDX, and five by on-axis SDD-EDX, followed by STEM EDX.

All of the Auger measurements were carried out with the PHI 700 Auger Nanoprobe at WUSTL, using a 10 kV, 10 nA beam rastered over the crater interiors. Spectrum acquisition consisted of three cycles over an energy range of 30–2130 eV for a total acquisition time of 2 min. These parameters were validated for determining residue compositions on the crater bottoms, if such residue is present, by measurements of an approximately 200 nm crater from a Stardust cometary foil. Measurements of adjacent regions of the Al foil were also made in order to assess the local composition of the foil and the presence of possible surface contaminants.

Conventional EDX measurements were performed on four craters on foil 1044N,1 and one on foil 1019W,1 with an Oxford Inca EDX system on the LEO 1530 FE-SEM at MPI. For crater 14, measurements were made at 20 kV to fully excite fluorescence from the Fe K, and Ce and Zn lines, and at 5 kV to limit the beam interaction volume to provide greater surface sensitivity. For craters 2, 9, 19, and 20, measurements were performed at 2 and 5 kV for maximum surface sensitivity. Measurements were made of the crater interiors, the craters including the rims, and regions of the foil adjacent to the craters.

On-axis, SDD-EDX measurements were performed at Sandia National Laboratory in Albuquerque, NM, with a custom Bruker detector attached to a Zeiss Supra 55VP FE-SEM. Craters 10 and 24 were measured at 5 and 20 kV. Craters 4, 6, 12, and 22 were measured at 2 and 5 kV. The custom SDD detector has a Be

window and requires use of mylar film attenuators for measurements above 5 kV. The data were acquired as spectrum images with the Bruker acquisition software, exported in Bruker RAW format and processed using the AXSIA multivariate statistical package.

Cross sections of the craters for STEM analysis were prepared by in situ FIB lift-out with an Ascend micromanipulator attached to the FEI Nova 600 FIB-SEM at NRL. The craters were protected with a cap of either carbon or Pt, deposited in situ with the electron beam at 5 kV, 1.6 nA prior to $Ga^+$ ion beam milling. Nominally 1 μm thick sections of the craters and surrounding foil were extracted with a W micromanipulator needle and welded with electron-beam-deposited Pt to Cu Omniprobe TEM support grids. The sections were milled to a thickness of approximately 150 nm, which is thicker than optimal for STEM analysis, but maximizes the amount of residue retained for subsequent analyses.

Transmission electron microcopy analysis was performed with a JEOL 2200FS equipped with a Noran System Six EDX system at the NRL. Bright-field TEM and high-angle annular dark-field STEM images were acquired. EDX data were acquired in STEM mode, as reduced-area raster spectrum acquisitions, and as spectrum images. The quantification of the spectra was performed with Cliff-Lorimer routines, taking into account absorption corrections for light elements, on an oxide basis for all elements other than S. Instrumental K factors were obtained for Mg, Si, and Fe using San Carlos olivine standards. Quantification of S, Ni, Ca, Cr, Zn, Ce, and Ti was based on default K factors.

Proof-of-concept oxygen isotope measurements were made with the CIW NanoSIMS 50L ion microprobe on three analogs of potential interstellar grain crater residues. The analog samples consisted of FIB-extracted cross sections of two craters from Stardust cometary foil 2043N,1 (Stroud et al. 2010a) and one crater (21) from Interstellar Collector foil 1033N,1, previously determined to contain only secondary ejecta from an impact on the solar cell array (see below). In order to minimize instrumental artifacts associated with measurements of cross sections suspended on Omniprobe grids, the crater FIB sections were first cut free from the Omniprobe grids and attached by FIB-based Pt-welding to gold-foil-covered Al stubs. A thin Au coat was deposited on the mount to mitigate possible charging effects in the SIMS measurements. Measurements were made with a <1 pA, approximately 100 nm diameter $Cs^+$ primary ion beam and multicollection of $^{12}C^-$, $^{16}O^-$, $^{17}O^-$, $^{18}O^-$, $^{28}Si^-$, $^{32}S^-$, and $^{27}Al^{16}O^-$ secondary ions and secondary electrons in imaging mode. All three samples contained O surface contamination outside the area of crater

residue, and this was used to normalize O-isotopic ratios to correct for instrumental mass fractionation and possible different detection efficiencies of the electron multipliers used to collect the O-isotope signals. Isotopic images were quantitatively analyzed with the L'image software (L. Nittler, CIW). Errors are completely dominated by counting statistics.

**Classification of Interstellar Grain Candidates**

To provide a consistent classification scheme for candidate interstellar grain impacts in both foil and aerogel collection media (Westphal et al. 2014), the ISPE team determined four distinct levels of candidacy: level 0, a crater-like feature in either aerogel or foil; level 1, a feature confirmed with SEM imaging (foils) or optical imaging (aerogel) to be consistent with hypervelocity impact; level 2, a hypervelocity impact feature with detectable residue that is inconsistent with spacecraft debris, and (aerogel) a track direction consistent with a ISD trajectory models; level 3, a hypervelocity impact feature with residue that has non-solar oxygen isotope composition.

## RESULTS

Automated SEM imaging was completed for 15 foils, resulting in over $10^5$ individual recorded images. Analysis of the images was completed for 13, including 7 long foils and 6 short foils. The foil surface quality showed significant variation due to scratches and contamination with aerogel fragments, as observed in the level II optical images (Figs. 3 and 4). SEM images, e.g., Fig. 6, of these foils showed additional, submicrometer surface texture from the foil manufacturing process, including small impurities pressed into the foil, pits associated with plucking of foil impurities, and aerogel debris loosely sticking to the foil surface. Although these imperfections increased the difficulty of the automatic image acquisition and the image analysis, all of the foils showed analyzable collection surface areas. In total, we identified 25 crater features (Fig. 7) in images that covered 4.84 cm$^2$, approximately 5% of the total searchable foil collection surface. The crater shapes varied from circularly symmetric to asymmetric, with aspect ratios of 1–1.5. The equivalent diameters ranged from 0.28 to 2.20 μm. The craters were random in spatial distribution and orientation of asymmetry to within the limits of the counting statistics (Fig. 8; Table 1).

Auger spectra were obtained for 13 craters and adjacent regions of the Al foil (Fig. 9). All spectra show features corresponding to C, O, and Al. In some spectra from foil areas adjacent to craters, a small Fe peak was
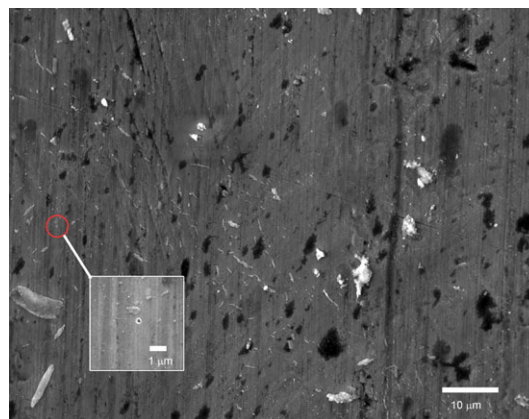


Fig. 6. Low magnification secondary electron SEM image (94 μm × 74 μm FOV) from foil 1092W,1, showing the identification of a crater feature (4, Table 3; Fig. 7) by the automated search software (Ogliore et al. 2012), despite the rough foil surface. The feature was confirmed as a 290 nm diameter crater, after re-imaging at 3× the original resolution (inset).

detected that can be attributed to Fe-rich impurities in the foil. One 1.2-μm crater (23) showed no other elements beyond those in the background spectra. The 12 other craters showed Si and one or more other elements, including Mg and/or Fe. Elements such as B, F, Ce, or Zn, which are strongly indicative of terrestrial or spacecraft contamination, were identified in the spectra from 6 craters. Ti and Na, which are present in solar cell cover glass, but are also possible extraterrestrial dust components, were tentatively detected in one crater each. The relative intensity of the Mg and Si features in different craters spanned a range from Mg ≪ Si to Mg ≫ Si. Fluorine was detected in two of the craters (13 and 16) that also showed the highest Mg/Si ratios.

Figure 10 shows the conventional SEM-EDX spectra for five craters. Multiple operating voltages were used in order to balance the energy range of the excited X-ray fluorescence with the analysis depth (see Table 2). As observed for the Auger measurements, all the EDX spectra show C, O, and Al. One crater (14) was measured during the first round of analyses using SEM operating voltages of 5 and 20 kV. The spectrum of this crater acquired at 5 kV (Fig. 10b) shows clear Fe L$_{\alpha 1}$ and Si K$_\alpha$ peaks, and possible F K$_\alpha$, Ce M$_{\alpha 1}$, Zn L$_{\alpha 1}$, and Mg K$_\alpha$ peaks. In the spectrum acquired at an operating voltage of 20 kV (Fig. 10a), which fully excites all of the relevant X-ray fluorescence peaks to a depth of approximately 3 μm, the Fe K$_\alpha$ peak is present, but there is no evidence for higher energy Ce L$_{\alpha 1}$ or Zn K$_\alpha$ peaks. Compared to the 5 kV spectrum, the 20 kV spectrum has a much higher Fe L$_{\alpha 1}$ peak intensity relative to the Si K$_\alpha$. Given the difference in
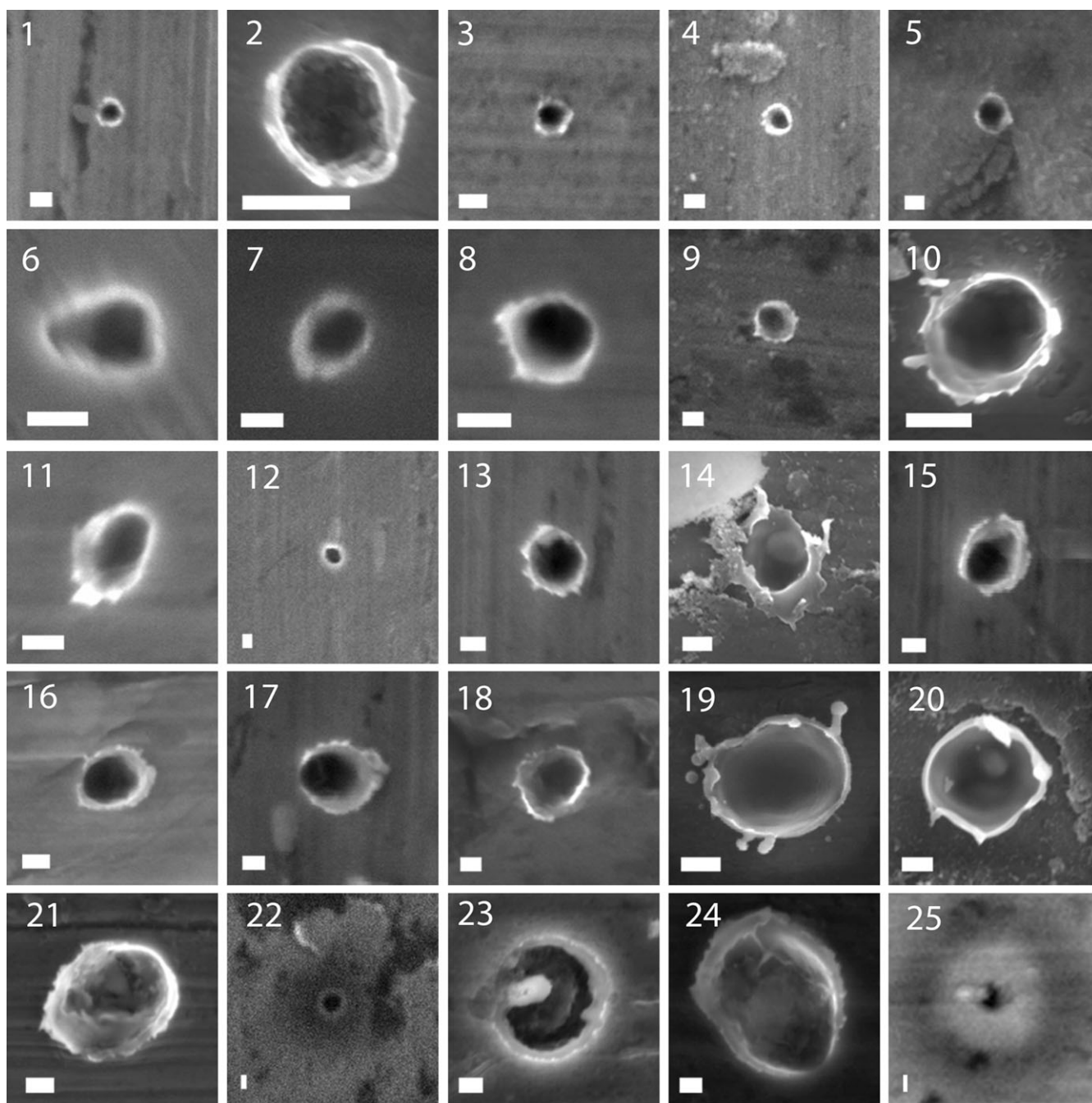
Fig. 7. SEM secondary electron images of the 25 identified craters. The scale bars are 0.25 μm.

excitation depth (see Table 2), the relative peak intensity variation indicates that significant subsurface Fe is present, but only surface Si. The other four craters were measured in the second round of analyses at SEM operating voltages of 2 and 5 kV. In the spectra acquired at 5 kV, all of the craters show a Si peak. Two of the craters (2 and 20) show clear evidence for an Fe L peak and two (9 and 19) show broad peaks in this energy range, suggestive of F and Ce. In addition,

crater 19 shows Mg and Zn or Na, crater 2 shows Mg, and crater 20 shows Ni. The spectra acquired at 2 kV show greatly attenuated Si and Al signals and lower background intensity, but peaks associated with Fe, Ce, Zn, or Na are not readily observed, possibly due to overall low counting statistics. Comparison of the 2 kV spectra of craters 20 (Fig. 10e) and 2 (Fig. 10g) shows that the Fe is spatially associated with O in crater 2, but not in crater 20.
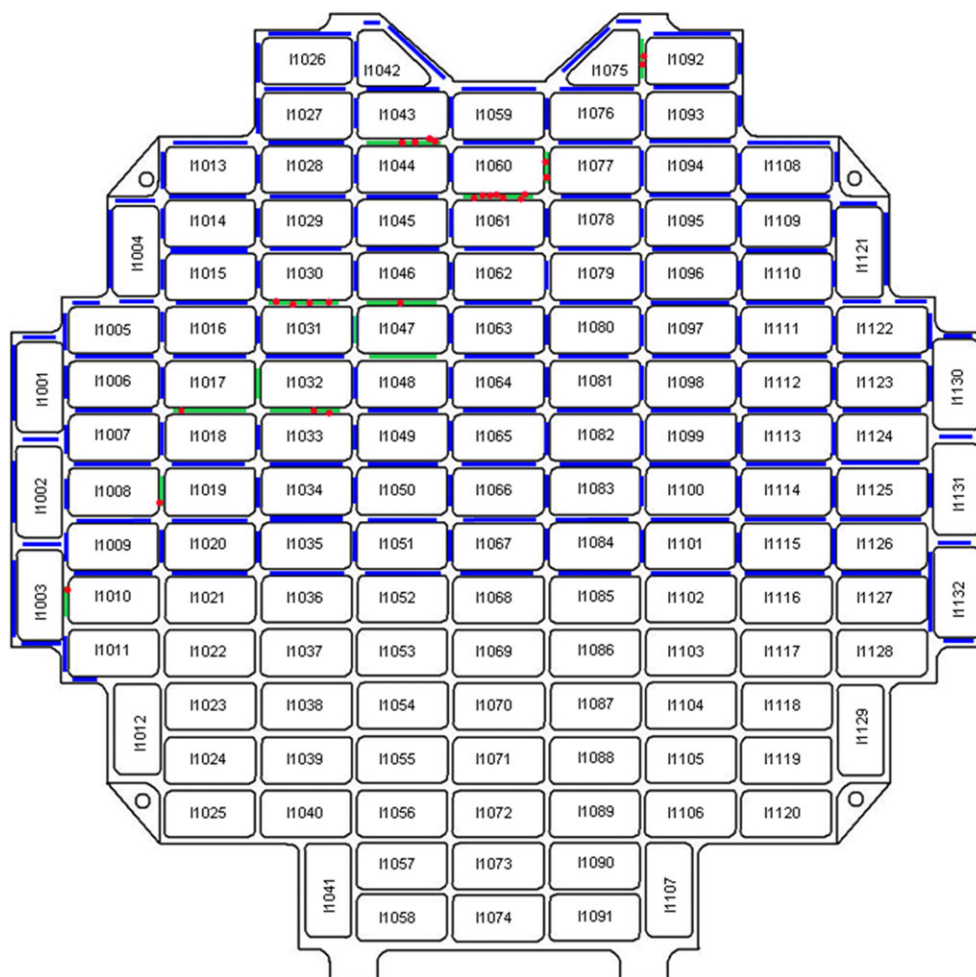
Fig. 8. Stardust Interstellar Tray schematic. Optical mosaic images of the foils shown in blue are available at the Stardust curation website (http://curator.jsc.nasa.gov/stardust/sample_catalog/Interstellar/Level2/Interstellar_Foil_Map.html). Foils for which scanning electron microscope mapping and image analysis is complete are shown in green. The approximate locations on the foils of the identified craters are indicated with red dots. (see online version for color figure.)

Table 2. Summary of effects of SEM operating voltage on EDX analysis of residues.

| Operating voltage (kV) | Estimated excitation depth (nm)[a] | Effect on EDX spectra of crater residues | Relevant peak energies (keV) |
|---|---|---|---|
| 2 | 60 | Provides the greatest surface sensitivity, with a reduced excitation of Al, so the signal is dominated by the residue; easier detection of minor elements with 0–1.3 keV X-ray peaks | C Kα 0.282, Ti Lα$_1$ 0.452, O Kα 0.523, F Kα 0.677, Fe Lα$_1$ 0.704, Ni Lα$_1$ 0.849, Ce Mα$_1$ 0.883, Na Kα 1.041, Zn Lα$_1$ 1.009, Mg Kα 1.254 |
| 5 | 300 | Full excitation of Al, Si, and S Kα lines. The high Al peak intensity can obscure the lower energy minor element peaks, but Si can be detected | Al Kα 1.487, Si Kα 1.740, S Kα 2.307 |
| 20 | 3000 | A greater portion of signal originates in the underlying Al foil, but the higher energy peaks can help with the identification of Ti, Ce, Fe, Ni, and Zn | Ti Kα 4.508, Ce Lα$_1$ 4.840, Fe Kα 6.400, Ni Kα 7.472, Zn Kα 8.631 |

[a]Excitation depth for a pure Al target estimated with Win X-ray simulation software (http://montecarlomodeling.mcgill.ca/software/winxray/winxray.html).
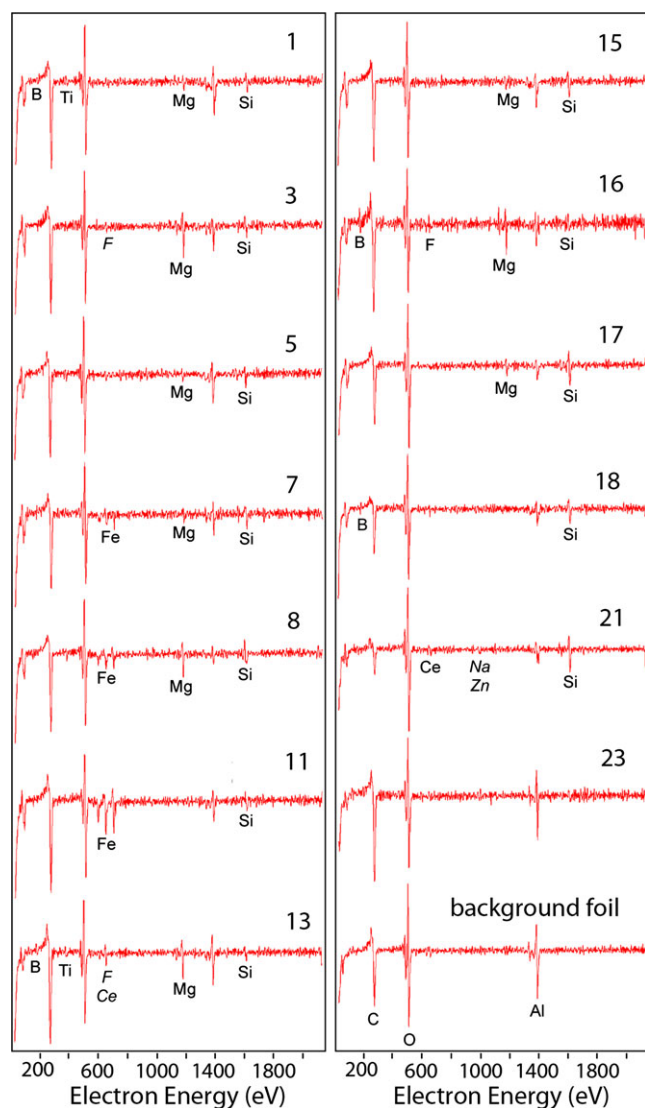
Fig. 9. Differentiated Auger spectra of 13 craters and a pristine region of an Al foil. C, O, and Al are present in all spectra but labeled only the background foil spectrum. Elements labeled in italics are tentative identifications.

For three craters (10, 22 and 24) the on-axis annular SDD SEM-EDX enabled mapping of the internal distribution of the residue with submicrometer spatial resolution. The principal component analysis (PCA) of crater 24 identified two components in the spectrum image (Fig. 11), one corresponding to the Al foil, and the other corresponding to a residue rich in Si, O, Mg, and possibly Na or Zn heterogeneously distributed in the crater interior. In the original SEM mapping image of crater 22 (see Fig. 7), the crater appeared to have a dark halo, and the crater interior was too dark to image any internal features. Re-imaged under better contrast conditions (Fig. 12), this crater

shows a large internal nodule. The PCA indicates that this nodule is an Fe-, C-, and O-rich impurity in the foil, rather than a true impact crater. Crater 10 is the smallest crater for which the SDD-EDX was able to map residue (Fig. 13). The PCA map of this crater shows Si- and O-rich residue on the interior of the crater rim, and also silica aerogel fragments distributed across the foil surface.

Scanning transmission electron microscopy (STEM) analysis of the FIB-extracted crater cross sections allows determination of the crater depth, and the thickness and composition of any retained residue. Crater 21 was cross sectioned after Auger analysis. The STEM-EDX analysis (Fig. 14) confirmed the Auger identification of Si, Ce, Zn, and also identified K, Ti, Fe, Mg, and possible F in the residue. The cross section of crater 20 (Fig. 15) shows it to be very shallow, with an approximate 1:4 depth:diameter ratio. The cross section also reveals that the crater intersected an $Al_3(Fe,Ni)$ impurity in the foil, which corresponds to the round, Fe-rich feature seen in the SEM analysis, and is consistent with the SEM-EDX data indicating metallic, rather than oxidized, Fe. The STEM-EDX analysis of craters 22 and 10 (Figs. 16 and 17) shows the presence of elements not detected with the SDD-EDX PCA analysis. For crater 22, F, Ce, Fe, Zn, Mg, K, and Ti, as well as Si and O were identified. For crater 10, Ce, Fe, and Ti, in addition to Si and O, were detected. The STEM analysis of the cross section of crater 23 (Fig. 18), revealed an Fe-rich internal grain, and feature dimensions inconsistent with an origin as an impact feature.

The results of all of the elemental analyses are summarized in Table 3, in order of increasing crater diameter. The majority of craters contain residue with a composition consistent with secondary impacts of fragments from the solar cell cover glass. Although the specific composition of the solar-cell cover-glass used on the Stardust spacecraft is proprietary information; it is known to be a similar glass to that used on the Hubble Space Telescope (HST). Microprobe analyses of fragments recovered during HST service missions SM-1 and SM-3B show variable compositions (elemental wt%): Na 3.21–3.41, Mg 0.63–0.66, Al 1.81–1.88, Si 31.86–32.15, K 2.27–2.39, Ca 1.13–1.21, Ti 0.67–0.78, Zn 3.81–3.87, Ba 1.23–1.29, Ce 3.63–3.86, O 42.6–43.0 (Kearlsey 2004). Unlike the HST, the cover glass on the Stardust solar array was coated with a MgF antireflection thin film (Burchell et al. 2012), so varying amounts of Mg, F, and Si may be present in a secondary impact crater, depending of the ratio of antireflection coating to glass in the impacting debris fragment. Two craters, with diameters of approximately 1–2 μm, contain indigenous Fe-C-O rich foil impurities, rather than true impacts. Two other
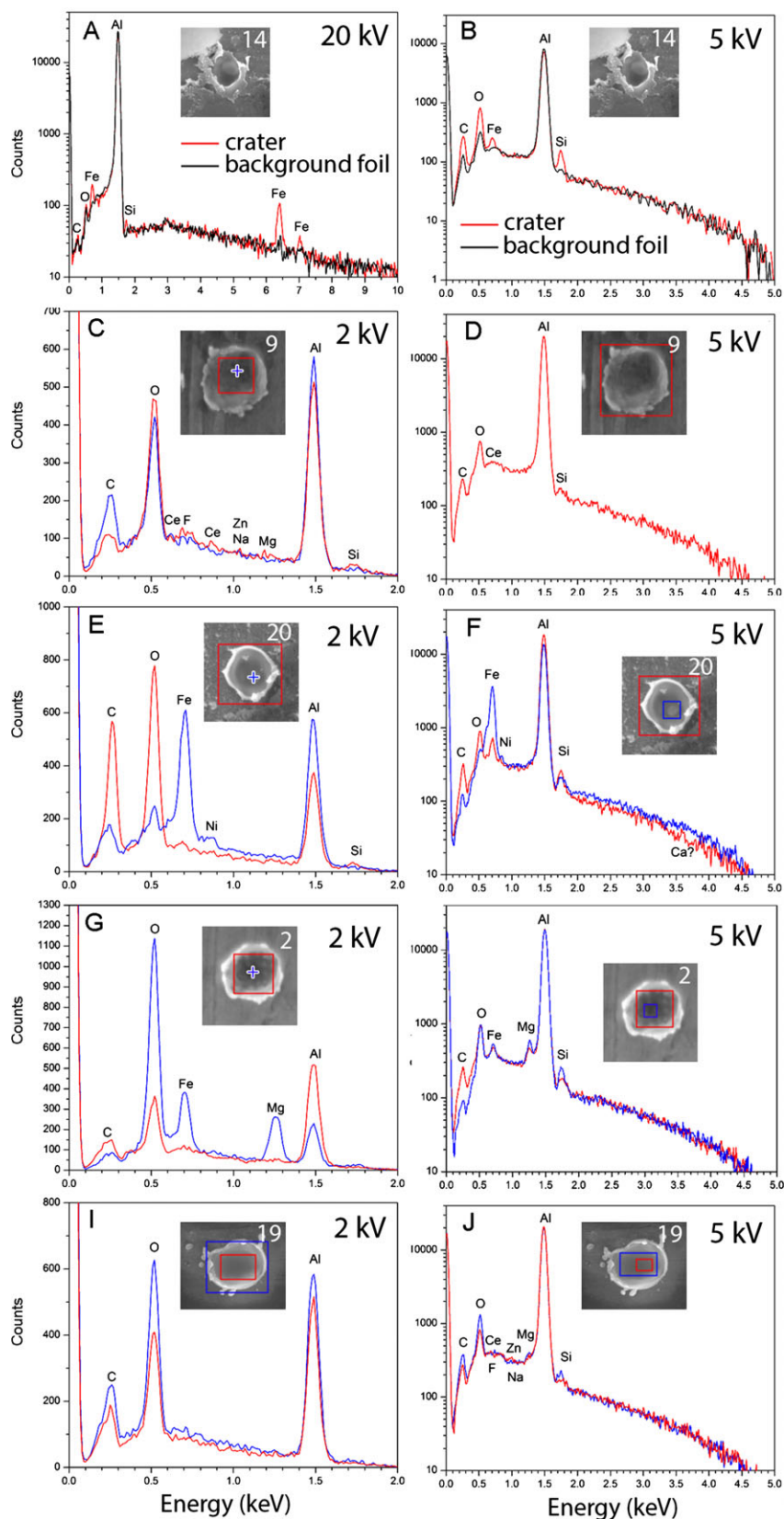
Fig. 10. Conventional Si(Li) SEM–EDX spectra of craters 2, 9, 14, 19, and 20. The colored boxes indicate the area analyzed for the corresponding colored spectra.
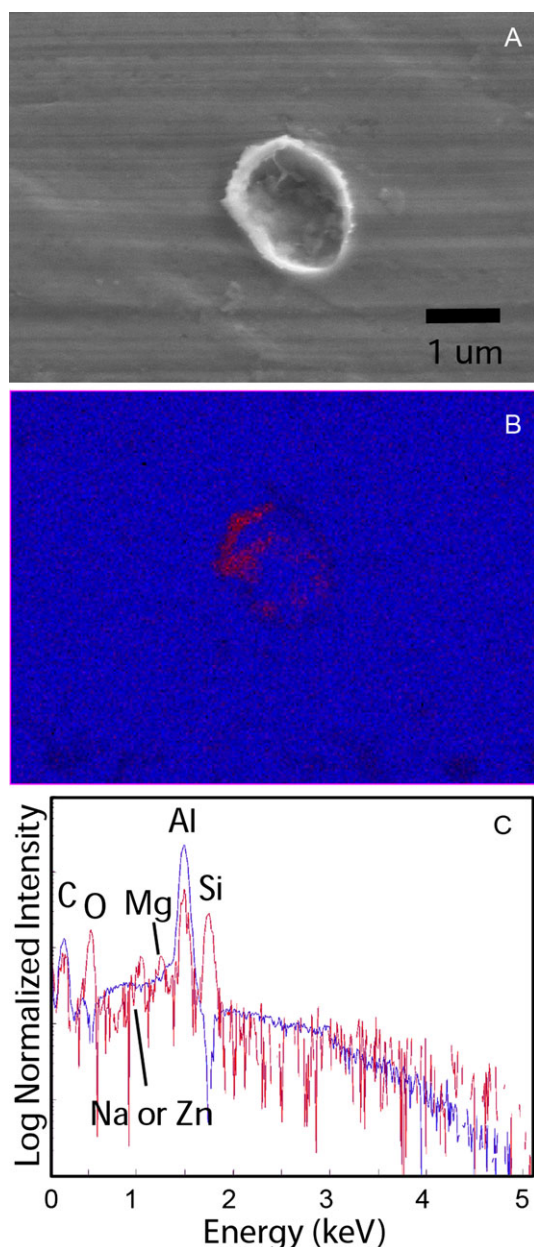
Fig. 11. On-axis, annular SDD SEM–EDX principal component analysis (PCA) of crater 24. a) Secondary electron image of the crater, with internal morphology indicative of a heterogeneous distribution of residue. b) Two-component PCA map of the crater and surrounding foil. c) X-ray spectra of the two components. The impactor residue (red) is rich in Si, Mg, O and possibly Na or Zn, and the foil (blue) shows Al and C. (see online version for color figure.)

craters show no detectable residue, and are likely pits resulting from the removal of precipitates during the foil manufacturing. As discussed in the next section, four craters show compositions consistent with a cosmic origin.

In principle, oxygen isotope measurements would be a useful method for distinguishing impacts made by
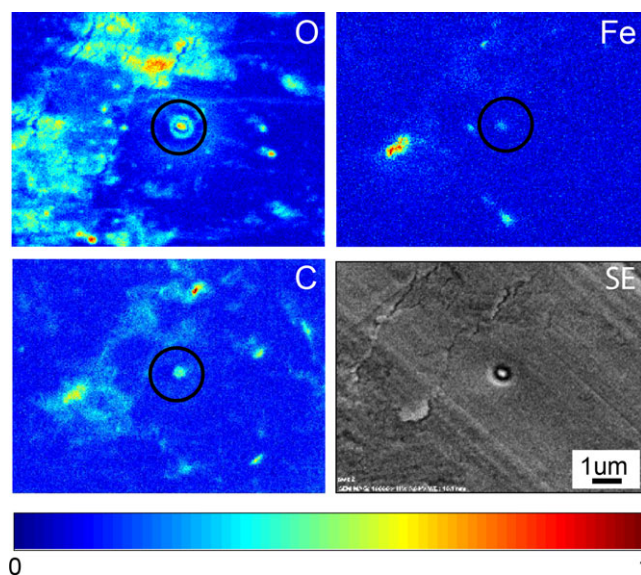


Fig. 12. On-axis, annular SDD SEM–EDX principal component analysis and secondary electron image of crater 22. The O, Fe, and C component maps shown were extracted from the full EDX spectrum image using Axsia multivariate statistical analysis software package. The color scale is normalized so that blue and red are the respective minimum and maximum concentrations for each component. These maps show that the crater is due to an Fe–C–O defect in the foil, not an impact. (see online version for color figure.)

grains of interstellar rather than solar system origin. However, the small volume of residue retained in the craters poses a serious constraint on the counting statistics that can be achieved, even with NanoSIMS techniques. In order to evaluate the feasibility of these measurements for candidate interstellar craters, we performed trial measurements of three FIB-sections: two craters from foil 2043N,1 from the Stardust cometary tray (Stroud et al. 2010a) and crater 21, which was determined to be of solar-cell cover-glass secondary origin. Two of the three craters had sufficient residue that two sub-regions could be defined and their O-isotopic ratios determined; for the third, ratios were determined for the total residue. The measured O isotope compositions of the five measurements of three samples are indistinguishable from solar system values (Fig. 19) with 1-$\sigma$ errors (dominated by counting statistics) of 20–40‰ for $\delta^{18}O$ and 40–80‰ for $\delta^{17}O$ values. Despite these large errors, the crater residues are clearly distinguished (see Fig. 19) from estimates of the isotopic composition of local interstellar medium, $\delta^{18}O = -104 \pm 50‰$, $\delta^{17}O = 300 \pm 75‰$ (Wilson 1999). This demonstrates that O-isotopic ratio measurements are feasible on small amounts of crater residue with sufficient precision to distinguish materials formed in the local ISM from those formed in the solar system.
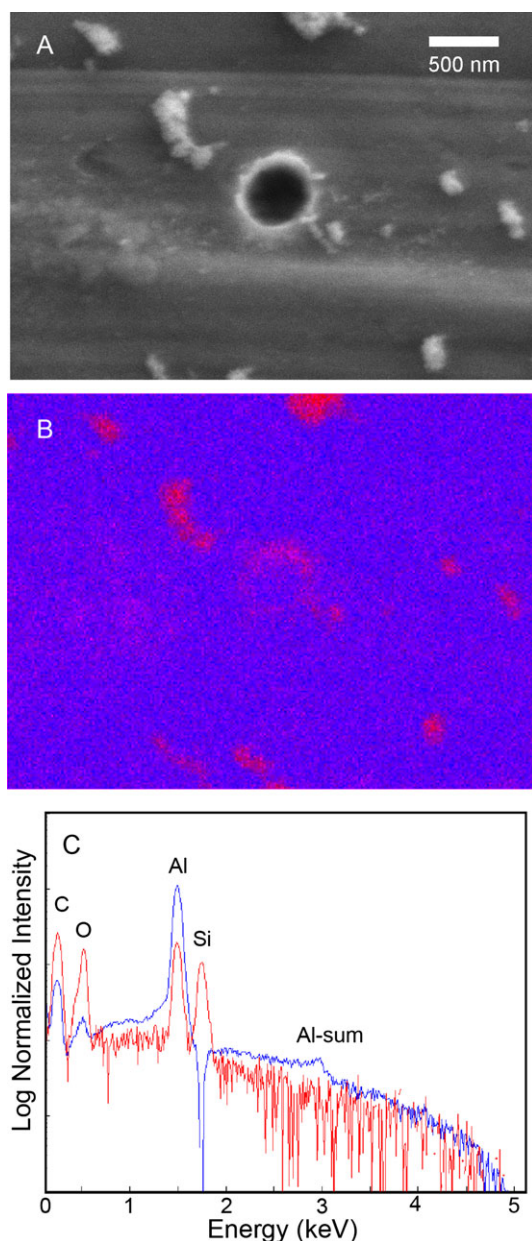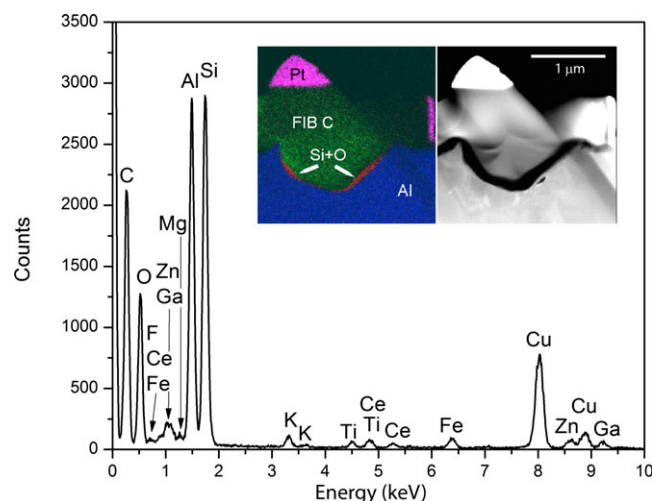
Fig. 14. STEM-EDX spectrum, elemental map (inset, left) and dark-field STEM image (inset, right) of the cross section of crater 21. The spectrum confirms the presence of Ce and the Zn tentatively identified by Auger spectroscopy, which confirms that the residue is solar cell cover glass. The Ga and Cu peaks are associated with the FIB processing and Cu TEM grid, respectively.



Fig. 13. On-axis, annular SDD SEM–EDX principal component analysis of crater 10. a) Secondary electron image. b) Two component principal component analysis map and c) X-ray spectra of the two components. The foil component is shown in blue, and a Si- and O-rich component is shown in red. The red component includes impactor residue at the rim of the crater, and aerogel fragments on the foil surface.
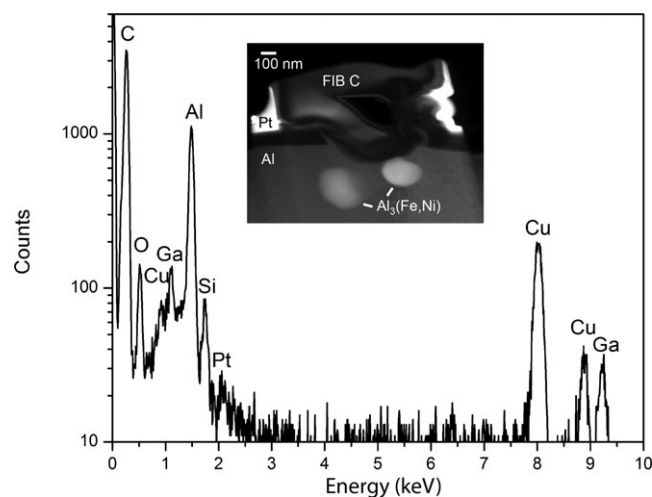


Fig. 15. STEM-EDX spectrum and dark-field image (inset) of the cross section of crater 20. The cross-section image reveals that the crater is very shallow, and has intersected an $Al_3(Fe, Ni)$ impurity in the underlying foil. The impactor residue, measured at the left side of the crater, shows only Si and O. The Ga, Cu, and Pt peaks are associated with the focused ion beam processing and Cu TEM grid.

## DISCUSSION

The fundamental goal of this work is to distinguish true extraterrestrial impact crater features on the Stardust Interstellar foils from impact features resulting from spacecraft debris, and from crater-like defects in the foils, so that candidate interstellar grain impacts can

be identified for further analysis. Unlike the tracks formed by particles in aerogel, the impact craters in the Al foils do not record a uniquely interpretable morphological signature of the particle trajectory, which can be matched to the interstellar wind flux during capture. As demonstrated by studies of laboratory-analog impact craters (Kearsley et al. 2012) and the Stardust cometary craters, asymmetric craters can result
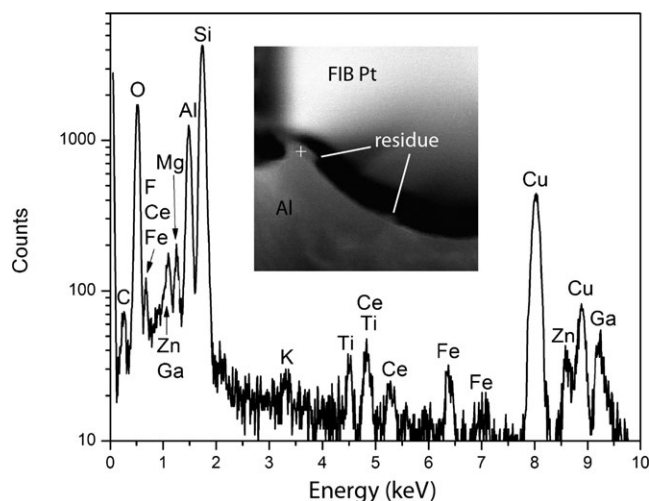
Fig. 16. STEM-EDX point spectrum and dark-field STEM (inset) of the cross section of crater 24. The analysis point is indicated with the + symbol. The residue has a composition indicative of solar cell cover glass: F, Ce, Zn, Mg, Si, K, Ti, and Fe. The Ga and Cu peaks are associated with the FIB processing and Cu TEM grid, respectively.



Fig. 18. STEM-EDX analysis of the cross section of crater 23. The elemental maps are shown as computed net count maps. The high-angle annular dark-field (HAADF) image shows that the crater morphology is inconsistent with a true impact crater. An Fe-rich particle extends from the right side of the cross section, above a 50 nm thick layer of oxidized Al that covers a void in the foil substrate.
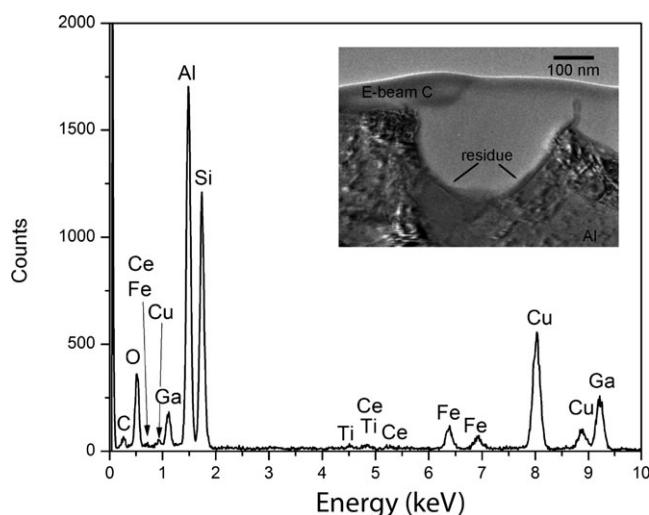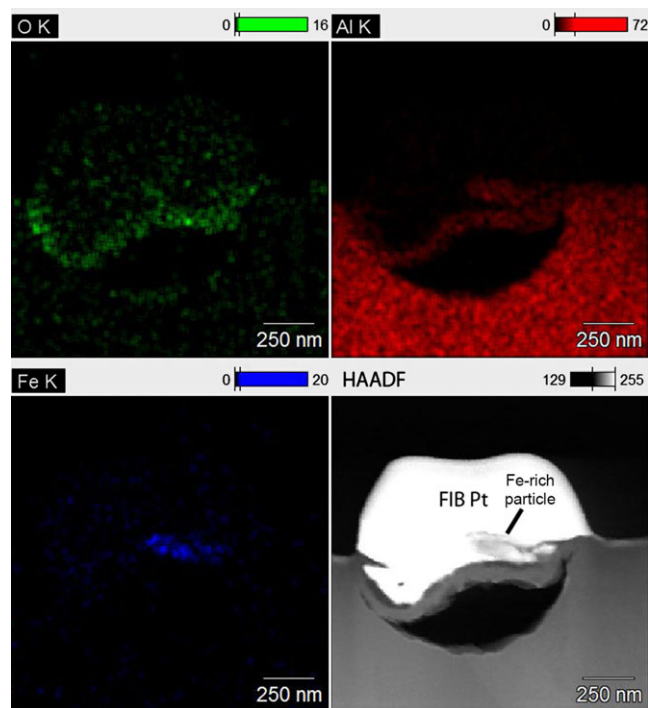


Fig. 17. STEM-EDX spectrum and bright-field TEM image (inset) of the cross section of crater 10. The residue contains Ti and Ce in addition to Si and Fe, indicative of solar cell cover glass. The Ga and Cu peaks are associated with the FIB processing and Cu TEM grid, respectively.

from either an oblique impact, or normal, or near-normal, incidence impact of a particle with a highly nonspherical shape, e.g., a needle or whisker, or an aggregate grain. Similarly, prior analog (Kearsley et al. 2012) and cometary crater studies (Leroux et al. 2008, 2010; Stroud et al. 2010a) showed that the crater depth is a function of impact velocity, particle composition, density, and simple or aggregate structure. Lower velocity impacts, lower density particles, and/or those

with a higher volatile content, such as organic particles, all produce shallower craters. Given the current uncertainty in the distribution of the shape, velocity, and composition of contemporary ISD, there is a considerable uncertainty as to what crater morphologies might result from ISD impacts. Thus, SEM imaging alone is useful for locating crater features, but in most cases does not provide a definitive answer as to the origin of the impacting grain. Identifying features that are unquestionably not interstellar in origin is a much more straightforward task.

The one class of crater-like features that can be definitively identified by imaging alone is the crater-like Fe-rich foil defect (22, 23, and 25), which is not a true impact feature. These defects have a round shape approximately 1 to 2 μm in diameter, with a large interior particle that is sometimes connected to the edge of the crater (23 and 25). The Al foil surrounding these defects can appear dark, due to the presence of carbon. Similar features have been observed on the Stardust cometary foils, and are thought to be a result of the foil manufacturing process (Kearsley et al. 2007). In cross-section STEM imaging (Fig. 18), these interior Fe particles do not show the characteristic crater-wetting,

Table 3. Summary of residue elemental analyses.

| Crater ID[a] | Diameter (μm) | Elements detected[b] Auger | SEM-EDX | STEM-EDX |
|---|---|---|---|---|
| 1) 1031N,1 37@02 | 0.24 | B,Mg,Si,Ti,Ce | n.m. | n.m. |
| **2) 1044N,1 12a_0277** | **0.28** | **n.m.** | **Mg,Si,Fe[1]** | **Mg,Si,Fe** |
| 3) 1061N,1 41@33 | 0.29 | *F*,Mg,Si | n.m. | n.m. |
| 4) 1092W,1 4_3 | 0.29 | n.m. | n.d.[2] | *Mg*,Si,Ti,Fe,*Ce* |
| 5) 1061N,1 22@44 | 0.35 | Mg,Si | n.m. | n.m. |
| 6) 1033N,1 5_71 | 0.35 | n.m. | n.d.[2] | n.d. |
| **7) 1061N,1 36@33** | **0.37** | **Mg,Si,Fe** | **n.m.** | **Mg,Si,S,Fe,Ca,Cr** |
| **8) 1061N,1 69@22** | **0.39** | **Mg,Si,Fe** | **n.m.** | **Mg,Si,S,Fe,Ni** |
| 9) 1044N,1 34_0317 | 0.44 | n.m. | Si, *Ce, Zn,Na*[1] | n.m. |
| 10) 1092W,1 5_29 | 0.45 | n.m. | Si[2] | Si,Na,Ti,Zn,Ce |
| **11) 1061N,1 135@30** | **0.46** | **Si,Fe** | **n.m.** | **Mg,Si,S,Fe,Ni,*Ca,Cr*** |
| 12) 1010W,1 12_7 | 0.46 | n.m. | n.d.[2] | n.d. |
| 13) 1031N,1 158@35 | 0.56 | B,*F*,Mg,Si,Ti,*Ce* | n.m. | n.m. |
| 14) 1044N,1 06e_0143 | 0.58 | n.m. | Si,Fe[1] | n.m. |
| 15) 1031N,1 239@11 | 0.61 | Mg,Si | n.m. | n.m. |
| 16) 1061N,1 205@32 | 0.63 | B,Si,Ce,Mg | n.m. | n.m. |
| 17) 1031 216@45 | 0.65 | Mg,Si | n.m. | n.m |
| 18) 1061 188@24 | 0.66 | Si,B | n.m. | n.m. |
| 19) 1019W,1 01e_0002 | 0.74 | n.m. | F,Mg,Si,*Na,Zn,Ce*[1] | n.m. |
| 20) 1044N,1, 06e_251 | 0.84 | n.m. | Si,Fe,Ni[1] | Si,Fe,Ni-impurity |
| 21) 1033N,1 11_175 | 1.0 | Si,*Na*,Ce,Zn | n.m. | Mg,Si,K,Ti,Fe,Zn,Ce |
| 22)1077W,1 499 | 1.1 | n.m. | Fe[2] | Fe |
| 23) 1047N,1 177@14 | 1.2 | n.d. | n.m. | Fe |
| 24) 1077W,1 387 | 1.6 | n.m. | Si,*Ce,Zn,Na*[2] | Mg,Si,K,Fe,Ti,Zn,Ce |
| 25) 1018N,1 1_560 | 2.2 | n.m. | Fe | n.m. |

[a]The level 2 interstellar crater candidates, 2, 7, 8, and 11, shown in bold, were assigned official names of: I1044N,3, 1061N,3, I1061N,4, and I1061N,5, respectively.

[b]Elements listed in italics are tentative identifications. Al, C, and O were detected in all analyses in addition to the elements listed. The labels n.d. and n.m. refer to none detected and not measured, respectively. Superscripts 1 and 2 refer to the conventional Si(Li) detector SEM-EDX measurements and the on-axis SDD SEM-EDX measurements, respectively.

conformal morphology indicative of melting that occurs for metal grain impacts at >5 km s$^{-1}$.

Other indigenous defects in the Al foils that were previously identified in the Stardust cometary foils are Al$_3$(Fe,Ni) precipitates (Kearsley et al. 2007; Leroux et al. 2008). These precipitates have a melting point of approximately 1160 °C, well above that of the Al (660 °C), and thus are more resistant to impact melting than the Al. As a result, an impact that intersects an Al$_3$(Fe,Ni) precipitate can produce a crater in the Al foil, while still preserving the precipitate. The retained precipitates are sometimes visible as a round particle in the crater interior (14 and 20). Of course, either interstellar particle or secondary debris impacts could intersect the precipitates, so further elemental analysis is required to make a determination of the origin of the impacting particle in such cases.

An unequivocal identification of the origin of a crater as the secondary impact of a fragment of solar panel debris is possible with either AES or SEM-EDX for 1/3 of the craters (Table 3). The residues of secondary solar cell array fragments impactors span a range of compositions, due to differences in the amount of MgF antireflection coating relative to solar-cell cover-glass present in different debris fragments, and whether or not an Al$_3$(Fe,Ni) precipitate was impacted. The Ni/Fe ratio of the precipitates themselves varies from 0 to about 0.1. This variable composition of the secondary impactors is evident in the varying peak heights of these elements in the Aueger spectra and SEM-EDX spectra. The cosmic abundance of Ce, F, and B is low enough that their detection by Auger spectroscopy or SEM-EDX in submicrometer particles is an indication of terrestrial origin. Zn is also of low cosmic abundance, but does occur as discrete (Fe,Zn)S particles in some IDPs (Christofferson and Buseck 1985; Rietmeijer 1989) and, thus, can be reasonably inferred to be terrestrial in origin only if S is not detected. Detection of one or more of the elements Mg, Si, and Fe without Ce, F, Zn, or B is not a definitive result, as these three elements are abundant in both cosmic dust and the solar cell panel materials. A null detection by
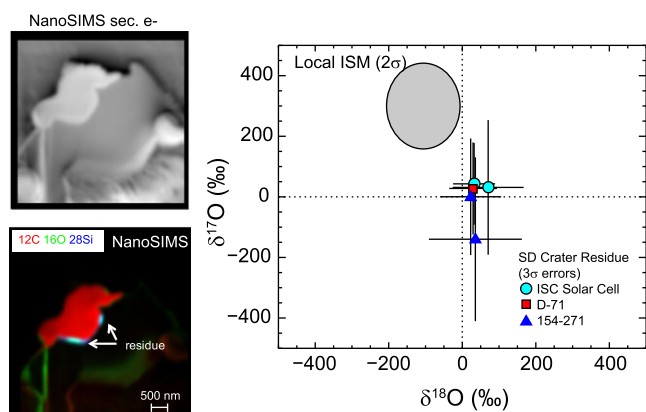
Fig. 19. NanoSIMS O-isotope data for Stardust crater FIB cross sections. Left: Secondary electron (top) and composite secondary ion (bottom; red = $^{12}$C, green = $^{16}$O, blue = $^{28}$Si) images for solar-cell cover-glass crater 21. Two areas of preserved projectile residue are clearly visible. Protective C deposited in crater by the focused ion beam is visible as large C-rich area. Right: O 3-isotope plot for residue in two Stardust cometary craters (Stroud et al. 2010a) and in crater 21. Plotted values are ‰ deviations from average measured O contamination on samples; error bars are 3-σ, based on counting statistics. The measured values are within errors of terrestrial values and are clearly distinct from astronomical estimates of the local interstellar medium (gray ellipse; Wilson 1999). (see online version for color figure.)

Auger spectroscopy or SEM-EDX is also nondiagnostic as this could simply reflect a volume of retained residue that is below detection limits.

One important result of this study is that SEM-EDX, as well as Auger spectroscopy, is useful for identifying the major element composition of the impactor residues. This can be attributed to the relatively large volumes of retained residue (tens of nanometers thick, rather than the a priori expectation of <10 nm) from impacting particles, which in turn is consistent with impact velocities of <15 km s$^{-1}$. Auger spectroscopy is better able to detect B and F, at least for the two EDX detectors used in this study, which incorporated an ultrathin polymer window (Si(Li) detector) and a Be window (on-axis quad SDD). However, both Auger spectroscopy and SEM-EDX were able to detect residues, when present, in craters as small as 0.29 μm. The use of low operating voltage, e.g., 2 kV, for the SEM-EDX acquisition is helpful for limiting the excitation volume to increase the relative X-ray signal from the impactor residue compared to the underlying Al foil (Fig. 10; Table 2). At 2 kV, the Al Kα X-ray signal is not fully excited and the bremsstrahlung background is greatly reduced, so that the fully excited Ce M, Zn L, Fe L, F K, Na K, and Mg K peaks can be more easily observed (Fig. 10). At 5 kV, both the Al K and Si K peaks are fully excited, but the Al K peak counts are >10 × higher than any

other element, so that minor elements in the residue can be observed only on a log scale. At higher voltage, e.g., 20 kV (Fig. 10a), the K peaks of Fe, Zn, Ti, and the Ce L peaks are fully excited, but the greater interaction volume of the higher energy electrons reduces the sensitivity to the surface residue. Comparison of the signal at different voltages can be particularly helpful for determining if Fe counts are due to a surface residue or an underlying precipitate. For example, the Fe-rich impurity of crater 14 is easily detected in both the 20 and 5 kV spectra, whereas the Si-rich impactor residue is prominent at 5 kV and barely observable at 20 kV. Similarly, the Fe L/Al K peak height ratio of the retained precipitate in crater 20 is approximately 1 for 2 kV acquisition, and approximately 1/8 for 5 kV (Figs. 10e and 10f, blue), whereas for the Fe-bearing residue in crater 2 (Figs. 10g and 10h, blue), the ratios are 2 and 1/20, respectively. Although for these spectra the comparison is complicated by a difference in acquisition geometry (spot versus box raster), the increased interaction volume at 5 kV yields a much greater relative reduction in Fe L peak intensity for the thin residue than for the precipitate.

Approximately half of the located craters require cross sectional STEM analysis in order to rule out a secondary debris impact origin. These craters either show no detectable residue, or only elements of ambiguous provenance, i.e., Mg, Si, and Fe in the Auger spectroscopy or SEM-EDX spectra. The lateral resolution of field-emission STEM-EDX measurements is of order 1 to 5 nm, so even very thin layers of residue are sufficient for measurement of minor elements. Of the nine craters analyzed by STEM that we determined to be impacts rather than foil defects, eight of them contained additional elements not detected by prior Auger spectroscopy or SEM-EDX measurements. This includes five craters in which solar cell debris signatures were clearly detected, and four in which no evidence for solar-cell cover-glass was found (labeled in bold in Table 3). The composition of the residues in the four cover-glass-free craters is consistent with a primary extraterrestrial origin: three are Mg-Fe silicate + Fe-Ni metal and sulfide, and one is Mg-Fe- silicate without sulfide. Based on these composition data, we identify these four craters as level 2 candidate ISD grain impacts. Notably, no craters with mixed residues with both cover-glass and sulfide were observed. This is consistent with laboratory simulations that indicate a large angular separation, and difference in velocity between primary and secondary ejecta plumes.

In addition to the high sensitivity and spatial resolution elemental analysis, the cross section STEM studies allow determination of diagnostic crater shape information, such as the depth-diameter ratio and the

crater floor symmetry. The five solar-cell cover-glass craters analyzed in cross section have symmetric crater floors, indicative of a single, dense impacting grain, and depth/diameter ratios of 0.3–1. By comparison with laboratory studies and computer simulations of normal incidence impacts of soda lime glass spheres, the velocity of the impacting dust grains can be estimated to be approximately 5 km s$^{-1}$ (Price et al. 2010, 2012). Of the four candidate interstellar craters, two showed double-well crater floors, indicative of an impacting grain composed of at least two distinct subgrains, in agreement with the STEM-EDX data for these craters showing both sulfide and silicate components. The best constraint on the velocities of these impacts comes from comparison with the Stardust cometary craters with similar composition residues, and cross-section measurements of analog craters produced by Van de Graaf acceleration of μm-sized silicate grains at velocities of approximately 25 km s$^{-1}$. The impact velocity of the cometary impact craters is well constrained at 6.1 km s$^{-1}$, and the crater depth: diameter ratio varies from approximately 0.5–1, with the shallower craters produced by aggregate impacting grains and those with high volatile content, i.e., C and S (Hörz et al. 2006; Leroux et al. 2008, 2010; Stroud et al. 2010a). From these comparisons, we can infer that the interstellar candidate craters were made by particles traveling at approximately 5–10 km s$^{-1}$, up to possibly 15 km s$^{-1}$ for crater 2. No craters have yet been observed with aspect ratios >1 that would more likely result from higher velocity impacts, i.e., >20 km s$^{-1}$. In particular, no evidence for any solar-wind accelerated nanoparticles traveling at hundreds of km s$^{-1}$ is observed (Meyer-Vernet et al. 2009).

The inferred impact speeds of the candidate interstellar grains are consistent with the speeds of the candidate interstellar particles found in the aerogel (Westphal et al. 2014). The calculated trajectory distribution of the ISD stream (Sterken et al. 2014) indicates that in order to impact the interstellar tray these grains have β values, the ratio of solar radiation pressure to the solar gravitational pressure, of about 1.5.

Assuming all four level 2 candidate craters are due to ISD particle impacts, we calculate the fluence of submicrometer ISD to be 0.74 cm$^{-2}$. This fluence is within an order of magnitude of the prior predictions of the fluence (approximately 0.13 cm$^{-2}$), based on in situ measurements from the Ulysses spacecraft (Landgraf et al. 1999). Thus, the measured and predicted fluence agreement is well within the experimental uncertainties. Landgraf et al. (1999) predicted that four times more sub-μm radius ISD particles than interplanetary dust particles would be collected, which indicates these four grains are more likely of interstellar rather than

interplanetary origin. It should be cautioned, however, that the flux of individual dust grains of either interplanetary or interstellar origin with sub-μm grain size is poorly constrained. It is somewhat surprising that three of the level 2 candidate craters are located on one foil, 1061N,1, and that this foil also has a large number of secondary impact features. However, this may reflect a bias in the crater detection statistics, i.e., that craters of all origins are easier to locate on large flat foils with less aerogel debris coverage. Furthermore, the areal density of secondary impact craters (Table 1) on the two foils with candidate IS craters (1061N,1: 0.26– 11 cm$^{-2}$; 1044N,1: 2.6–12 cm$^{-2}$) is in statistical agreement with the average secondary crater density of 1.6–4.4 cm$^{-2}$ within 1σ uncertainty (Gehrels 1986), taking into account the random fluctuations in the sparse statistics. Finally, the three IS candidate craters themselves were not spatially clustered on foil 1061N,1 and are each distinct in elemental composition, giving support for an origin as individual interstellar grains. Still, without isotopic composition data inconsistent with a solar system origin, we cannot rule out the possibility that the three candidate IS craters on 1061N,1, or the one on 1044N,1, originated in the solar system.

## CONCLUSIONS

The Al foils from the Stardust interstellar tray provide a unique opportunity for direct laboratory analysis of individual particles from the contemporary ISD stream. The low IS dust flux, the condition of the foils, and the background of secondary impact features from solar cell debris fragments are all major challenges to the identification of true ISD impact features. We have located three crater-like features that are associated with Fe impurities in the Al foil, two that appear to be pits associated with the plucking of foil impurities during foil manufacture, and >11 craters that contain residue indicative of solar cell debris. We also have located four impact craters with residue elemental compositions and crater morphologies consistent with the impact of submicrometer grains of interstellar origin, which we designate level 2 interstellar candidates. The total abundance of collected candidate ISD is in general agreement with prior calculations. Details of the analyses of these candidate interstellar impact craters, including oxygen isotopic composition measurements, will be presented elsewhere.

*Editorial Handling*—Dr. A. J. Timothy Jull

## REFERENCES

Borg J., Hörz F., Bridges J. C., Burchell M. J., Djouadi Z., Floss C., Graham G. A., Green S. F., Heck P. R., Hoppe P., Huth J., Kearsley A., Leroux H., Marhas K., Stadermann F. J., and Teslich N. 2007. SEM-EDS analyses of small craters in stardust aluminium foils: Implications for the Wild-2 dust distribution (abstract #1592). 38th Lunar and Planetary Science Conference. CD-ROM.

Brownlee D., Tsou P., Aleon J., Alexander C. M. O'D., Araki T., Bajt S., Baratta G. A., Bastien R., Bland P., Bleuet P., Borg J., Bradley J. P., Brearley A., Brenker F., Brennan S., Bridges J.C., Browning N. D., Brucato J. R., Bullock E., Burchell M. J., Busemann H., Butterworth A., Chaussidon M., Cheuvront A., Chi M. F., Cintala M. J., Clark B. C., Clemett S. J., Cody G., Colangeli L., Cooper G., Cordier P., Daghlian C., Dai Z. R., D'Hendecourt L., Djouadi Z., Dominguez G., Duxbury T., Dworkin J. P., Ebel D. S., Economou T. E., Fakra S., Fairey S. A. J., Fallon S., Ferrini G., Ferroir T., Fleckenstein H., Floss C., Flynn G., Franchi I. A., Fries M., Gainsforth Z., Gallien J. P., Genge M., Gilles M. K., Gillet P., Gilmour J., Glavin D. P., Gounelle M., Grady M. M., Graham G. A., Grant P. G., Green S. F., Grossemy F., Grossman L., Grossman J. N., Guan Y., Hagiya K., Harvey R., Heck P., Herzog G. F., Hoppe P., Hörz F., Huth J., Hutcheon I. D., Ignatyev K., Ishii H., Ito M., Jacob D., Jacobsen C., Jacobsen S., Jones S., Joswiak D., Jurewicz A., Kearsley A. T., Keller L. P., Khodja H., Kilcoyne A. L. D., Kissel J., Krot A., Langenhorst F., Lanzirotti A., Le L., Leshin L. A., Leitner J., Lemelle L., Leroux H., Liu M. C., Luening K., Lyon I., MacPherson G., Marcus M. A., Marhas K., Marty B., Matrajt G., McKeegan K., Meibom A., Mennella V., Messenger K., Messenger S., Mikouchi T., Mostefaoui S., Nakamura T., Nakano T., Newville M., Nittler L. R., Ohnishi I., Ohsumi K., Okudaira K., Papanastassiou D.A., Palma R., Palumbo M. E., Pepin R.O., Perkins D., Perronnet M., Pianetta P., Rao W., Rietmeijer F. J. M., Robert F., Rost D., Rotundi A., Ryan R., Sandford S. A., Schwandt C. S., See T. H., Schlutter D., Sheffield-Parker J., Simionovici A., Simon S., Sitnitsky I., Snead C. J., Spencer M. K., Stadermann F. J., Steele A., Stephan T., Stroud R., Susini J., Sutton S. R., Suzuki Y., Taheri M., Taylor S., Teslich N., Tomeoka K., Tomioka N., Toppani A., Trigo-Rodriguez J. M., Troadec D., Tsuchiyama A., Tuzzolino A. J., Tyliszczak T., Uesugi K., Velbel M., Vellenga J., Vicenzi E., Vincze L., Warren J., Weber I., Weisberg M., Westphal A. J., Wirick S., Wooden D., Wopenka B., Wozniakiewicz P., Wright I., Yabuta H., Yano H., Young E. D., Zare R. N., Zega T., Ziegler K., Zimmerman L., Zinner E., and Zolensky M. 2006. Research article—Comet 81P/Wild 2 under a microscope. *Science* 314:1711–1716.

Burchell M. J., Cole M. J., Price M. C., and Kearsley A. T. 2012. Experimental investigation of impacts by solar cell secondary ejecta on silica aerogel and aluminum foil: Implications for the Stardust Interstellar Dust Collector. *Meteoritics & Planetary Science* 47:671–683.

Christofferson R. and Buseck P. R. 1985. Mineralogy of the "olivine" IR class of interplanetary dust. Proceedings, 16th Lunar and Planetary Science Conference. pp. 127–128.

Floss C., Allen C., Armes S., Bajt S., Ball A., Bastien R., Bechtel H., Borg J., Brenker F. E., Bridges J. C., Brownlee D. E., Burchell M. J., Burghammer M., Butterworth A., Chater R., Cloetens P., Cody G., Davis A., Doll R., Ferroir T., Flynn G., Frank D., Gainsforth Z., Grün E., Heck P. R., Hillier J., Hoppe P., Hörz F., Howard L., Hudson B., Huss G. R., Huth J., Kearsley A. T., Lai B., Landgraf M., Leitner J., Lemelle L., Leroux H., Nittler L., Ogliore R., Postberg F., Price M. C., Sandford S., Schmitz S., Silversmit G., Simionovici A., Srama R., Stadermann F. J., Stephan T., Stroud R., Sutton S., Toucoulou R., Trieloff M., Trigo-Rodríguez J., Tsou P., Tsuchiyama A., Tyliczszak T., Vekemans B., Vincze L., Warren J., Westphal A. J., and Zolensky M. E. 2010. Preliminary examination of Al foil I1061N,1 from the Stardust Interstellar Collector (abstract #5270). *Meteoritics & Planetary Science* 45:A55.

Floss C., Allen C., Bajt S., Bechtel H. A., Borg J., Brenker F., Bridges J., Brownlee D. E., Burchell M., Burghammer M., Butterworth A. L., Cloetens P., Davis A. M., Doll R., Flynn G. J., Frank D., Gainsforth Z., Grün E., Heck P. R., Hillier J. K., Hoppe P., Howard L., Huss G. R., Huth J., Kearsley A., King A. J., Lai B., Leitner J., Lemelle L., Leonard A., Leroux H., Nittler L. R., Ogliore R. C., Ong W. J., Postberg F., Price M. C., Sandford S. A., Sans Tresseras J. A., Schmitz S., Schoonjans T., Schreiber K., Silversmit G., Siminonovici A., Srama R., Stadermann F. J., Stephan T., Stodolna J., Stroud R. M., Sutton S. R., Toucoulou R., Trieloff M., Tsou P., Tsuchiyama A., Tyliczszak T., Vekemans B., Vincze L., Westphal A. J., and Zolensky M. E., and > 29,000 Stardust@home dusters. 2011. Stardust Interstellar foils I1061N,1 and I1031N,1: First results from automated crater searches and future analytical possibilities (abstract #1576). 42nd Lunar and Planetary Science Conference. CD-ROM.

Gehrels N. 1986. Confidence limits for small number events in astrophysical data. *The Astrophysical Journal* 303: 336–346.

Heck P. R., Hoppe P., and Huth J. 2012. Sulfur four isotope NanoSIMS analysis of comet-81P/Wild 2 dust in impact craters on aluminum foil C2037N from NASA's Stardust mission. *Meteoritics &Planetary Science* 47:649–659.

Hörz F. 2012. Cratering and penetration experiments in aluminum and teflon: Implications for space-exposed surfaces. *Meteoritics & Planetary Science* 47:763–797.

Hörz F., Bastien R., Borg J., Bradley J. P., Bridges J. C., Brownlee D. E., Burchell M. J., Chi M. F., Cintala M. J., Dai Z. R., Djouadi Z., Dominguez G., Economou T. E., Fairey S. A. J., Floss C., Franchi I. A., Graham G. A., Green S. F., Heck P., Hoppe P., Huth J., Ishii H., Kearsley A. T., Kissel J., Leitner J., Leroux H., Marhas K., Messenger K., Schwandt C. S., See T. H., Snead C., Stadermann F. J., Stephan T., Stroud R., Teslich N., Trigo-Rodríguez J. M., Tuzzolino A. J., Troadec D., Tsou P., Warren J., Westphal A., Wozniakiewicz P., Wright I., and Zinner E. 2006. Impact features on Stardust: Implications for comet 81P/Wild 2 dust. *Science* 314:1716–1719.

Kearlsey A. T. 2004. Technical note 3: Post-flight impact anlaysis of HST solar arrays—2002 retrieval. Submitted to European Space Agency under contract no. 16283/NL/LvH.

Kearsley A. T., Graham G. A., Burchell M. J., Cole M. J., Dai Z. R., Teslich N., Bradley J. P., Chater R., Wozniakiewicz P. A., Spratt J., and Jones G. 2007. Analytical scanning and transmission electron microscopy of laboratory impacts on Stardust aluminum foils: Interpreting impact crater morphology and the composition of impact residues. *Meteoritics & Planetary Science* 42:191–210.

Kearsley A. T., Borg J., Graham G. A., Burchell M. J., Cole M. J., Leroux H., Bridges J. C., Hörz F., Wozniakiewicz P. J., Bland P. A., Bradley J. P., Dai Z. R., Teslich N., See T., Hoppe P., Heck P. R., Huth J., Stadermann F. J., Floss C., Marhas K., Stephan T., and Leitner J. 2008. Dust from comet Wild 2: Interpreting particle size, shape, structure, and composition from impact features on the Stardust aluminum foils. *Meteoritics & Planetary Science* 43:41–73.

Kearsley A. T., Westphal A. J., Stadermann F. J., Armes S. P., Ball A. D., Borg J., Bridges J. C., Brownlee D. E., Burchell M. J., Chater R. J., Davis A. M., Floss C., Flynn G., Gainsforth Z., Grün E., Heck P., Hoppe P., Hörz F., Howard L. E., Howe G., Huss G. R., Huth J., Landgraf M., Leitner J., Leroux H., Nittler L., Ogliore R., Postberg F., Price M. C., Srama R., Stroud R., Trieloff M., Trigo-Rodríguez J., Sandford S. A., Stephan T., Sternovsky Z., Tsou P., and Zolensky M. E. 2010. Finding interstellar particle impacts on Stardust aluminium foils: The safe handling, imaging and analysis of samples containing femtogram residues (abstract #1593). 41st Lunar and Planetary Science Conference. CD-ROM.

Kearsley A. T., Burchell M. J., Price M. C., Cole M. J., Wozniakiewicz P. J., Ishii H. A., Bradley J. P., Fries M., and Foster N. J. 2012. Experimental impact features in Stardust aerogel: How track morphology reflects particle structure, composition, and density. *Meteoritics & Planetary Science* 47:737–762.

Landgraf M., Müller M., and Grün E. 1999. Prediction of the in-situ dust measurements of the stardust mission to comet 81P/Wild 2. *Planetary and Space Science* 47:1029–1050.

Leitner J., Hoppe P., and Heck P. R. 2010a. First discovery of presolar material of possible supernova origin in impact residues from Comet 81P/Wild 2 (abstract #1607). 41st Lunar and Planetary Science Conference. CD-ROM.

Leitner J., Allen C., Armes S., Bajt S., Ball A., Bastien R., Bechtel H., Borg J., Brenker F. E., Bridges J. C., Brownlee D. E., Burchell M. J., Burghammer M., Butterworth A.,

Chater R., Cloetens P., Cody G., Davis A., Ferroir T., Floss C., Flynn G., Frank D., Gainsforth Z., Grün E., Heck P. R., Hillier J., Hoppe P., Hörz F., Howard L., Hudson B., Huss G. R., Huth J., Kearsley A. T., Lai B., Landgraf M., Lemelle L., Leroux H., Nittler L., Ogliore R., Price M. C., Postberg F., Sandford S., Schmitz S., Silversmit G., Simionovici A., Srama R., Stadermann F., Stephan T., Stroud R., Sutton S., Toucoulou R., Trieloff M., Trigo-Rodríguez J., Tsou P., Tsuchiyama A., Tyliczszak T., Vekemans B., Vincze L., Warren J., Westphal A. J., and Zolensky M. E. 2010b. Preliminary examination of the Stardust Interstellar Collector: Al foil I1044N,1 (abstract #5292). *Meteoritics & Planetary Science* 45:A116.

Leroux H., Stroud R. M., Dai Z. R., Graham G. A., Troadec D., Bradley J. P., Teslich N., Borg J., Kearsley A. T., and Hoerz F. 2008. Transmission electron microscopy of cometary residues from micron-sized craters in the Stardust Al foils. *Meteoritics & Planetary Science* 43:143–160.

Leroux H., Kearsley A. T., and Troadec D. 2010. Mineralogy of Wild 2 residues in micron-sized craters from the Stardust Al-foils (abstract #1621). 41st Lunar and Planetary Science Conference. CD-ROM.

McKeegan K. D., Aleon J., Bradley J., Brownlee D., Busemann H., Butterworth A., Chaussidon M., Fallon S., Floss C., Gilmour J., Gounelle M., Graham G., Guan Y. B., Heck P. R., Hoppe P., Hutcheon I. D., Huth J., Ishii H., Ito M., Jacobsen S. B., Kearsley A., Leshin L. A., Liu M. C., Lyon I., Marhas K., Marty B., Matrajt G., Meibom A., Messenger S., Mostefaoui S., Mukhopadhyay S., Nakamura-Messenger K., Nittler L., Palma R., Pepin R. O., Papanastassiou D. A., Robert F., Schlutter D., Snead C. J., Stadermann F. J., Stroud R., Tsou P., Westphal A., Young E. D., Ziegler K., Zimmermann L., and Zinner E. 2006. Isotopic compositions of cometary matter returned by Stardust. *Science* 314:1724–1728.

Meyer-Vernet N., Maksimovic M., Czechowski A., Mann I., Zouganelis I., Goetz K., Kaiser M. L., St. Cyr O. C., Bougeret J. L., and Bale S. D. 2009. Dust detection by the wave instrument on STEREO: Nanoparticles picked up by the solar wind? *Solar Physics* 256:463–474.

Ogliore R. C., Butterworth A. L., Doran A., Gainsforth Z., Scholl A., Westphal A. J., and Young A. 2010. Photoemission electron microscopy of Stardust cometary foils (abstract #2572). 41st Lunar and Planetary Science Conference. CD-ROM.

Ogliore R. C., Floss C., Stadermann F. J., Kearsley A. T., Leitner J., Stroud R. M., and Westphal A. J. 2012. Automated searching of Stardust interstellar foils. *Meteoritics & Planetary Science* 47:729–736.

Postberg F., Allen C., Bajt S., Bechtel H. A., Borg J., Brenker F. E., Bridges J., Brownlee D. E., Burchell M., Burghammer M., Butterworth A. L., Cloetens P., Davis A. M., Doll R., Floss C., Flynn G. J., Frank D., Gainsforth Z., Grün E., Heck P. R., Hillier J. K., Hoppe P., Howard L., Huss G. R., Huth J., Kearsley A., King A. J., Lai B., Leitner J., Lemelle L., Leonard A., Leroux H., Nittler L. R., Ogliore R. C., Ong W. J., Price M. C., Sandford S. A., Sans Tresseras J. A., Schmitz S., Schoonjans T., Schreiber K., Silversmit G., Simionovici A., Srama R., Stephan T., Stodolna J., Stroud R. M., Sutton S. R., Toucoulou R., Trieloff M., Tsou P., Tsuchiyama A., Tyliczszak T., Vekemans B., Vincze L., Westphal A. J., and Zolensky M. E. 2011. High fidelity studies of Interstellar Dust analogue

impacts in Stardust aerogel and foil (abstract #5447). *Meteoritics & Planetary Science* 46:A191.

Price M. C., Kearsley A. T., Burchell M. J., Hörz F., Borg J., Bridges J. C., Cole M. J., Floss C., Graham G., Green S. F., Hoppe P., Leroux H., Marhas K. K., Park N., Stroud R., Stadermann F. J., Telisch N., and Wozniakiewicz P. J. 2010. Comet 81P/Wild 2: The size distribution of finer (sub-10 mm) dust collected by the Stardust spacecraft. *Meteoritics & Planetary Science* 45:1409–1428.

Price M. C., Kearsley A. T., Burchell M. J., Howard L. E., Hillier J. K., Starkey N. A., Wozniakiewicz P. J., and Cole M. J. 2012. Stardust interstellar dust calibration: Hydrocode modeling of impacts on Al-1100 foil at velocities up to 300 km s$^{-1}$ and validation with experimental data. *Meteoritics & Planetary Science* 47:684–695.

Rietmeijer F. J. M. 1989. Ultrafine-grained mineralogy and matrix chemistry of olivine-rich chondritic interplanetary dust particles. Proceedings, 19th Lunar and Planetary Science Conference. pp. 513–521.

Stadermann F. J. and Floss C. 2008. Determining the elemental and isotopic makeup of cosmic dust from residues in impact craters: Preparation for the ISPE (abstract #5105). *Meteoritics & Planetary Science* 43:A147.

Stadermann F. J., Hoppe P., Floss C., Heck P. R., Hörz F., Huth J., Kearsley A. T., Leitner J., Marhas K. K., McKeegan K. D., and Stephan T. 2008. Stardust in Stardust—The C, N, and O isotopic compositions of Wild 2 cometary matter in Al foil impacts. *Meteoritics & Planetary Science* 43:299–313.

Stadermann F. J., Floss C., Lam H. Y. M., Price M. C., Burchell M. J., and Kearsley A. T. 2010. Identifying off-normal hypervelocity impacts in aluminum foil by Auger imaging: Implications for the examination of the Interstellar Collector (abstract #1349). 40th Lunar and Planetary Science Conference. CD-ROM.

Sterken V. J., Westphal A. J., Altobelli N., Grün E., Postberg F., Srama R., Allen C., Anderson D., Ansari A., Bajt S., Bastien R. S., Bassim N., Bechtel H. A., Borg J., Brenker F. E., Bridges J., Brownlee D. E., Burchell M., Burghammer M., Butterworth A. L., Changela H., Cloetens P., Davis A. M., Doll R., Floss C., Flynn G., Frank D., Gainsforth Z., Heck P. R., Hillier J. K., Hoppe P., Hudson B., Huth J., Hvide B., Kearsley A., King A. J., Lai B., Leitner J., Lemelle L., Leroux H., Leonard A., Lettieri R., Marchant W., Nittler L. R., Ogliore R., Ong W. J., Price M. C., Sandford S. A., Tresseras J. S., Schmitz S., Schoonjans T., Silversmit G., Simionovici A., Solé V. A., Stephan T., Stodolna J., Stroud R. M., Sutton S., Trieloff M., Tsou P., Tsuchiyama A., Tyliszczak T., Vekemans B., Vincze L., Korff J. V., Wordsworth N., Zevin D., Zolensky M. E., and >30,000 Stardust@home dusters. 2014. Stardust Interstellar Preliminary Examination X: Impact speeds and directions of interstellar grains on the Stardust Dust Collector. *Meteoritics & Planetary Science*, doi:10.1111/maps.12219.

Stroud R. M., Koch I. M., Bassim N. D., Piccard Y. N., and Nittler L. R. 2010a. Structure and composition of comet Wild 2 residues in sub-micron to micron-sized craters (abstract #1792). 40th Lunar and Planetary Science Conference. CD-ROM.

Stroud R. M., Allen C., Armes S., Bajt S., Ball A., Bastien R., Bechtel H., Borg J., Brenker F. E., Bridges J. C.,

Brownlee D. E., Burchell M. J., Burghammer M., Butterworth A., Chater R., Cloetens P., Cody G., Davis A., Ferroir T., Floss C., Flynn G., Frank D., Gainsworth Z., Grün E., Heck P. R., Hillier J., Hoppe P., Hörz F., Howard L., Hudson B., Huss G. R., Huth J., Kearsley A. T., Lai B., Landgraf M., Leitner J., Lemelle L., Leroux H., Nittler L., Ogliore R., Price M. C., Postberg F., Sandford S., Schmitz S., Silversmit G., Simionovici A., Srama R., Stadermann F., Stephan T., Sutton S., Toucoulou R., Trieloff M., Trigo-Rodríguez J., Tsou P., Tsuchiyama A., Tyliczszak T., Vekemans B., Vincze L., Warren J., Westphal A. J., and Zolensky M. E. 2010b. Preliminary examination of Al foil I1077w,1 from the Stardust Interstellar Collector (abstract #5271). *Meteoritics & Planetary Science* 45:A198.

Stroud R. M., Allen C., Bajt S., Bechtel H. A., Borg J., Brenker F., Bridges J., Brownlee D. E., Burchell M., Burghammer M., Butterworth A. L., Cloetens P., Davis A. M., Floss C., Flynn G. J., Frank D., Gainsforth Z., Grün E., Heck P. R., Hillier J. K., Hoppe P., Howard L., Huss G. R., Huth J., Kearsley A., King A. J., Lai B., Leitner J., Lemelle L., Leroux H., Nittler L. R., Ogliore R. C., Postberg F., Price M. C., Sandford S. A., Sans Tresseras J. A., Schmitz S., Schoonjans T., Silversmit G., Simionovici A., Srama R., Stadermann F. J., Stephan T., Stodolna J., Sutton S. R., Toucoulou R., Trieloff M., Tsou P., Tsuchiyama A., Tyliczszak T., Vekemans B., Vicenze L., Westphal A. J., and Zolensky M. E. 2011. Identification of impact craters in foils from the Stardust Interstellar Dust Collector (abstract #1753). 41st Lunar and Planetary Science Conference. CD-ROM.

Tsou P., Brownlee D. E., Sandford S. A., Horz F., and Zolensky M. E. 2003. Wild 2 and interstellar sample collection and Earth return. *Journal of Geophysical Research* 108:3-1–3-21.

Westphal A. J., Allen C., Anderson D., Bajt S., Bechtel H. A., Borg J., Brenker F., Bridges J., Brownlee D. E., Burchell M., Burghammer M., Butterworth A. L., Cloetens P., Davis A. M., Floss C., Flynn G. J., Frank D., Gainsforth Z., Grün E., Heck P. R., Hillier J. K., Hoppe P., Howard L., Huss G. R., Huth J., Kearsley A., King A. J., Lai B., Leitner J., Lemelle L., Leroux H., Lettieri R., Lyverse P., Marchant W., Nittler L. R., Ogliore R. C., Postberg F., Price M. C., Sandford S. A., Sans Tresseras J. A., Schmitz S., Schoonjans T., Silversmit G., Simionovici A., Srama R., Stadermann F. J., Stephan T., Stodolna J., Stroud R. M., Sutton S. R., Toucoulou R., Trieloff M., Tsou P., Tsuchiyama A., Tyliczszak T., Vekemans B., Vincze L., von Korff J., Zevin D., Zolensky M. E., and > 29,000 Stardust@home dusters. 2014. Stardust Preliminary Examination 0: Final reports of the Stardust Interstellar Preliminary Examination. *Meteoritics & Planetary Science*, doi:10.1111/maps.12221.

Wilson T. L. 1999. Isotopes in the interstellar medium and circumstellar envelopes. *Reports on Progress in Physics* 62:143–185.

Wozniakiewicz P. J., Ishii H. A., Kearsley A. T., Burchell M. J., Bradley J. P., Price M. C., Teslich N., Lee M. R., and Cole M. J. 2012. Stardust impact analogs: Resolving pre- and postimpact mineralogy in Stardust Al foils. *Meteoritics & Planetary Science* 47:708–728.